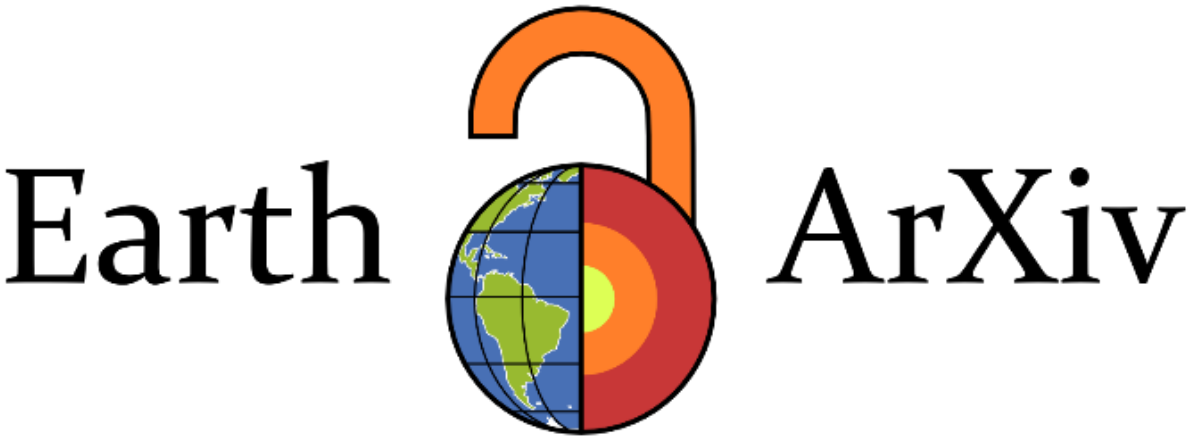

The effects of rain on a Ka-band swath altimeter: lessons learned from the SWOT mission

Bruno Picard[a] Aurélien Colin,[b] Romain Husson,[b] Gérald Dibarboure,[c]

[a] *Fluctus SAS, 2 rue Henri Prouho, 81800 Rabastens, France*

[b] *Collecte Localisation Satellites (CLS), Avenue la Pérouse, 29280 Plouzané, France*

[c] *Centre National d'Etudes Spatiales (CNES), 18 Avenue Edouard Belin, 31400 Toulouse, France*

Corresponding author: Bruno Picard, bpicard@satobsfluctus.eu

ABSTRACT: The Surface Water and Ocean Topography (SWOT) mission offers unprecedented Ka-band swath altimetry measurements via its KaRIn instrument, but remains highly sensitive to signal attenuation by precipitation. This study investigates the radiometric behavior of KaRIn under rain conditions, focusing on the characterization, correction, and physical interpretation of the normalized radar backscatter coefficient (σ_0). A three-regime decibel conversion scheme was implemented to handle linear σ_0 values, including negative returns, and a parametric angular correction model was applied based on wind-dependent polynomial fits. Cross-validation against KaPR (GPM) and AltiKa revealed consistent angular trends and wind dependencies, with systematic biases of +2.3 dB and +3.3 dB, respectively, over wind speeds ranging from 3 to 13 m/s, which account for over 85 % of oceanic conditions globally.

Two rainfall retrieval methods were developed from KaRIn σ_0: a physically-based attenuation inversion using the ITU-R γ–R relation, and a supervised random forest (RF) classifier trained with collocated NEXRAD ground radar measurements. The RF model achieved an overall accuracy of 89.2 %, with a detection probability of 82.5 % for rain rates above 5 mm/hr, compared to 72.4 % for the ITU approach. Global analysis confirms that rain rates exceeding 5 mm/hr or an attenuation of 10 dB result in significant degradation of KaRIn sea surface height (SSH) retrievals. Above this threshold, more than 95 % of SSH observations are rejected by Level-3 editing filters, validating the statistical relevance of the rain flag criterion.

Beyond SWOT, this study provides a methodological foundation for Ka-band altimetry in upcoming missions. The Sentinel-3 Next Generation (S3-NG) mission will benefit from these rain detection algorithms during post-launch calibration and data quality control. Similarly, the ODYSEA mission—a CNES–NASA Doppler scatterometer designed to resolve fine-scale vector winds and surface currents—will rely on accurate rain filtering to isolate geophysical signals. The statistical characterization of Ka-band attenuation and the rain retrieval strategies presented here are key to enabling reliable Ka-band remote sensing in dynamic meteorological environments.

SIGNIFICANCE STATEMENT: This Work has not yet been peer-reviewed and is provided by the contributing Author(s) as a means to ensure timely dissemination of scholarly and technical Work on a noncommercial basis. Copyright and all rights therein are maintained by the Author(s) or by other copyright owners. It is understood that all persons copying this information will adhere to the terms and constraints invoked by each Author's copyright. This Work may not be reposted without explicit permission of the copyright owner.

This work has been submitted to AMS JTECH.

This study addresses a major limitation in Ka-band altimetry: the degradation of radar signal under precipitation. Using data from the SWOT mission, we quantify the impact of rain on sea surface height measurements and propose two retrieval algorithms—one physical, one machine learning-based—to detect and characterize rain events. These methods enable accurate flagging of rain-contaminated data and provide essential tools for current and future satellite missions operating at Ka-band, including Sentinel-3 Next Generation and ODYSEA. Our results improve understanding of atmospheric effects on radar altimetry and support the design of more robust data quality controls.

1. Introduction

The Surface Water and Ocean Topography (SWOT) mission is a pioneering satellite initiative designed to provide unprecedented insights into Earth's water systems. Developed through an international collaboration involving NASA, CNES (Centre National d'Études Spatiales), the Canadian Space Agency (CSA), and the United Kingdom Space Agency (UKSA), the satellite was launched in December 2022. SWOT employs a Ka-band Radar Interferometer (KaRIn) to deliver high-resolution, two-dimensional measurements of water surface elevations, addressing the limitations of traditional nadir altimeters. The mission aims to advance the understanding of oceanographic and hydrological processes, including submesoscale ocean dynamics, river discharge, and changes in lake storage Fu et al. (2024); Dibarboure et al. (2024); Peral et al. (2024).

Early results from SWOT have demonstrated its capacity to capture small-scale ocean phenomena, such as mesoscale eddies and internal waves, along with volumetric changes in terrestrial water bodies. These findings illustrate the mission's potential to support climate change research and water resource management Dibarboure et al. (2024); Fu et al. (2024).

The mission's initial successes underscore its transformative role in global water monitoring. By providing high-resolution data, SWOT has laid the groundwork for diverse applications, ranging from coastal vulnerability assessments to hydrological modeling. Its unique capabilities offer promising new avenues for understanding Earth's water cycle and the ocean's contribution to climate regulation Peral et al. (2024); Fu et al. (2024); Dibarboure et al. (2024).

However, the mission faces significant challenges due to the attenuation of the Ka-band radar signal by precipitation, which is notably more sensitive to rain than the Ku-band used in earlier altimetry missions. As illustrated by Figure 1, rain-induced attenuation reduces the received signal-to-noise ratio (SNR) and can lead to errors in sea surface height (SSH) retrieval, particularly under heavy rainfall conditions. Unlike Ku-band altimeters, which exhibit lower sensitivity to atmospheric effects, Ka-band systems such as KaRIn on SWOT must address these challenges through advanced correction models and data flagging to maintain observation accuracy during adverse weather conditions Peral et al. (2024); Picard (2021).

This paper aims to assess the sensitivity of the SWOT Ka-band Radar Interferometer (KaRIn) to precipitation-induced signal attenuation and to propose robust methodologies for detecting and quantifying this effect. First, a comprehensive characterization of the KaRIn backscatter coefficient (σ_0) is conducted, including a novel three-regime decibel conversion and an angular correction derived from Ka-band precipitation radar models. Based on this radiometric foundation, two complementary rainfall retrieval approaches are introduced: a physically-based attenuation inversion using ITU-R models, and a supervised machine learning algorithm trained on collocated NEXRAD radar data. The validation of these methods is then carried out through comparisons with ground-based and satellite rainfall observations. Finally, the impact of precipitation on SWOT sea surface height (SSH) data availability is quantified, and an extrapolation of these findings is proposed for future Ka-band missions such as ODYSEA.

2. A review on the impact of precipitations on altimetry missions

a. Atmospheric attenuation of the radar signal

The propagation of radar signals through the atmosphere is subject to attenuation, primarily driven by the modification of the atmosphere's complex refractivity. This attenuation is governed by the imaginary part of the refractivity Liebe et al. (1993), which is influenced by various

atmospheric constituents, including atmospheric gases (oxygen as the dry component and water vapor as the wet component), clouds, and hydrometeors such as rain, snow, graupel, and ice.

The attenuation values presented correspond to two-way path attenuation at Ka-band frequencies. The dry component remains relatively stable, reaching a maximum of approximately 0.4 dB under high-pressure and cold atmospheric conditions. In contrast, the wet component exhibits greater variability, ranging from 0 dB in dry atmospheric conditions to approximately 2 dB in environments with high water vapor content Liebe et al. (1993); Lillibridge et al. (2014). Attenuation due to liquid water within clouds typically remains below 2 dB but can escalate to 5 dB in the presence of large cumulonimbus clouds Monaldo et al. (1986).

The most significant contributor to attenuation is precipitation. In radar altimetry, it is challenging to distinguish between hydrometeors; therefore, for the purposes of this analysis, all precipitation will be treated as rainfall. Rain-induced attenuation depends on both the rainfall rate and the height of the rain cell Monaldo et al. (1986); International Telecommunication Union Radiocommunication Sector (ITU-R) (2005). Attenuation can range from 1 dB for a rainfall rate of 2 mm/hr with a 1-km rain cell to as much as 50 dB for a rainfall rate of 20 mm/hr and a 5-km rain cell.

Although the impact of precipitation is less pronounced at Ku- and C-band frequencies, rain attenuation has consistently posed challenges for the availability and accuracy of altimetric measurements. This issue has been the subject of extensive investigation since the inception of satellite altimetry.

b. Historical Missions Using Ku and C Bands

The integration of precipitation effects into satellite altimetry began with pivotal studies on the attenuation of radar backscatter (σ_0) by rain. Early missions such as Seasat and TOPEX/Poseidon demonstrated the impact of rain on geophysical measurements, including significant wave height and sea surface height. Techniques developed during these missions utilized dual-frequency altimeters operating in the Ku and C bands to detect and mitigate rain-induced errors. The differential attenuation between these frequencies was critical in developing rain detection algorithms and refining altimetric accuracy (Srokosz, 1988; Guymer et al., 1995)Srokosz (1988); Guymer and Quartly (1995).

The TOPEX/Poseidon mission (1992) established the use of rain flags derived from departures in the Ku-C band σ_0 relationship to flag rain-contaminated data. Subsequent research by Tournadre and Quartly expanded these approaches, applying them to Jason-1 and Envisat altimeters. The algorithms proved effective in detecting rain-affected measurements while minimizing false positives (Tournadre, 1998; Quartly, 1998)Tournadre (1998); Quartly (1998).

c. The Transition to Ka Band and the AltiKa Mission

The SARAL/AltiKa mission, launched in 2013, marked a significant technological shift with its Ka-band radar altimeter operating at 35.75 GHz. This higher frequency offered improved spatial resolution and enhanced sensitivity to small-scale features, particularly in coastal and inland water regions. However, this sensitivity came with heightened challenges due to increased atmospheric attenuation from rain and clouds, approximately seven times larger than at the Ku band (Tournadre et al., 2009; Picard et al., 2021)Tournadre (2009); Picard (2021).

Jean Tournadre's analyses provided a detailed understanding of rain-induced waveform distortions at the Ka band. His modeling showed how rain cells, particularly those with high variability and intensity, could severely attenuate signals, causing geophysical parameter retrieval errors (Tournadre et al., 2009). To address this, innovative algorithms such as the Matching Pursuit (MP) rain flag were developed. This algorithm successfully identified short-scale distortions in waveforms, enabling accurate flagging of rain-affected dataTournadre (2009); Tournadre et al. (2015).

Building on this work, Bruno Picard introduced the Attenuation Cells Characterization Algorithm (ACECAL), which analyzed Ka-band backscatter time series to directly characterize rain cells. This approach revealed the internal structure of rain cells and quantified their impact on altimetric data availability. Picard's studies demonstrated the potential for integrating rain cell characterization into operational altimetry, providing valuable insights for future missions such as SWOT (Picard et al., 2021)Picard (2021).

3. Datasets description

a. SWOT products

The SWOT Low Resolution (LR) Sea Surface Height (SSH) Level-2 product, derived from the KaRIn swath instrument, serves as the primary dataset for this study. Comprehensive details

regarding the product specifications and quality assessments are available in Raynal et al. (2023); Bohé (2023); Chen (2023).

KaRIn data products are provided on grids with resolutions of 250 meters and 2 kilometers. This study focuses on the 2-km resolution grid. Each half-orbit is represented as an array, where the dimensions are determined by the number of lines in the along-track direction (approximately 10,000) and the number of cross-track pixels (69 pixels).

Theoretical incidence angles at the center of the 69 cross-track pixels (for the 2-km grid) span from -4.93° to +4.93°, with a sampling interval of approximately 0.145°.

In practice, no valid data are available for the nadir pixel. Additionally, data quality is compromised and falls below SWOT's performance requirements beyond the swath region extending from 10 km to 60 km on either side of the nadir Dibarboure et al. (2024); Peral et al. (2024). Consequently, the usable portion of the KaRIn swath consists of 56 pixels, with center incidence angles ranging from approximately 0.6° to 4.5° on both sides of the nadir.

This study primarily relies on the KaRIn backscatter coefficient, sigma_0. In accordance with recommendations from the SWOT Project documentation, the parameter `sig0_karin_2` is utilized. This parameter, as defined in the Level-2 products, represents the `Normalized radar cross-section (sigma0) from KaRIn in real, linear units (not decibels). The value may be negative due to noise subtraction. The value is corrected for instrument calibration and atmospheric attenuation. Atmospheric attenuation corrections are derived from a meteorological model (sig0_cor_atmos_model).`

As it is corrected for atmospheric attenuation computed from the European Center for Medium-Range Weather Forecasts (ECMWF) analysis, this sigma_0 inherently includes errors resulting from the temporal and spatial interpolation along the KaRIn swath of the two closest analyses, which are separated by six hours. Additional errors may also arise from the physical limitations of water vapor estimation within the model.

Nevertheless, considering that

- the amplitude of attenuation due to water vapor (approximately 2 dB in very wet atmospheric conditions Lillibridge et al. (2014)) is small compared to attenuation caused by precipitation, which can reach tens of dB,

- attenuation estimates provided by the radiometer are not yet mature in the current version of the products,

the decision is made to directly use the sigma_0 corrected for atmospheric attenuation computed from ECMWF data.

In the following, observations are considered valid if the following criteria are met:

- The quality flag `ssha_karin_2_qual` for the SSHA from KaRIn, (`ssha_karin_2`) is equal to zero.

- The dynamic ice flag at the location of the KaRIn measurement `dynamic_ice_flag`, is equal to zero.

- Due to certain limitations of the dynamic ice flag, an additional criterion is applied: for latitudes above 57° (North and South), observations where `ssha_karin_2_qual` is non-zero are discarded.

The validity flag extracted from the Level-3 products (`cvl_flag_val`, as defined by Dibarboure et al. Dibarboure et al. (2024), will also be utilized, as it enhances the detection of spurious pixels and outliers.

b. NEXRAD products

The NEXRAD (Next-Generation Radar) network is a system of Doppler weather radars deployed across the United States to provide high-resolution precipitation and storm tracking data Heiss et al. (1990); National Oceanic and Atmospheric Administration (2025). Operated by the National Weather Service (NWS), the Federal Aviation Administration (FAA), and the U.S. Air Force (USAF), NEXRAD offers rainfall estimates, hydrometeor classification, and severe weather monitoring with updates every 5 to 10 minutes National Centers for Environmental Information (2025). The data are widely used for weather forecasting, hydrological modeling, and the validation of satellite-based precipitation measurements. NEXRAD Level II data were downloaded through

the NOAA National Centers for Environmental Information (NCEI) data archive National Oceanic and Atmospheric Administration (2025); National Centers for Environmental Information (2025). The NEXRAD precipitation observations have been used in the following to define an algorithm for the retrieval of rainfall rate from KaRIn σ_0 and to validate it.

4. Characterization of KaRin backscattering coefficient

The challenges associated with the atmospheric attenuation of the backscatter coefficient and its relationship with precipitation rates require the use of a σ_0 expressed in decibels and corrected for geometric effects related to the incidence angle across the swath. The following paragraphs detail the methodology used to apply these corrections.

a. Conversion of the linear backscattering coefficient to decibels

The KaRIn σ_0 is stored in linear units in the products (noted σ_0^{lin} below). But since the relations between attenuation and radar signal are expressed in decibels a conversion is required. The difficulty is that negative values can occurred but, on the contrary to what is claimed in the metadata, this is not entirely due to "noise subtraction" but it is also clearly happening when atmospheric attenuation occurs. Typically, every pixels marked as green or yellow in Figure 1 (b) showing the KaRIn σ_0 already in decibels are converted from negative values of the initial linear σ_0, the minimum value being close to -0.09. So a specific approach is required to maintain consistency and numerical stability. The transformation follows three cases:

First, any values of σ_0^{lin} that fall below a predefined threshold MAX_LINEAR in absolute magnitude are considered unreliable and are flagged as non-valid (NaN):

$$\sigma_0^{\text{dB}} = \begin{cases} \text{NaN}, & \text{if } |\sigma_0^{\text{lin}}| \leq \text{MAX\_LINEAR} \end{cases} \tag{1}$$

For negative values of σ_0^{lin}, an alternative logarithmic transformation is applied to ensure a meaningful representation while preserving numerical consistency:

$$\sigma_0^{\text{dB}} = 2 \cdot 10\log_{10}(\text{MAX\_LINEAR}) - 10\log_{10}(-\sigma_0^{\text{lin}}) \tag{2}$$

This formulation prevents numerical errors and maintains a valid dynamic range.

For positive values of σ_0^{lin}, the conventional decibel conversion formula is applied:

$$\sigma_0^{\text{dB}} = 10\log_{10}(\sigma_0^{\text{lin}}) \tag{3}$$

In this study, a value of 10^{-3} is selected for MAX_LINEAR. With this approach, the negative value of -0.09 for the linear σ_0^{lin} converts to -49.5 dB. The consistency of the results presented below confirms that the choices made do not introduce any significant limitations in the conversion process.

b. Dependency of sigma$_0$ with the incidence angle and the ocean surface conditions

The geometric optics assumption regarding the impact of sea surface roughness on radar signals, combined with an isotropic Gaussian distribution for sea surface slopes, provides a simplified model for the backscattering coefficient sigma$_0$ Jackson et al. (1992):

$$\sigma_0 = \frac{|R|^2}{\text{mss}}\sec^4(\theta)\exp\left(-\frac{\tan^2(\theta)}{\text{mss}}\right) \tag{4}$$

where θ is the incidence angle, $|R|$ represents the Fresnel reflection coefficient, and mss is the mean square slope of the sea surface. This equation highlights the dependency of sigma$_0$ on the measurement geometry through θ, on sea surface temperature (SST) via the Fresnel coefficient, and on surface conditions such as wind speed, wind direction, and wave height through mss. Both the Fresnel coefficient and mss are also frequency-dependent.

The complex relationship between Ka-band sigma$_0$, surface state, and SST (along with comparisons to Ku-band sigma$_0$) is discussed in greater detail in Nouguier et al. (2016); Yan et al. (2019); Hossan and Jones (2021) (for wind speed and Significant Wave Height, SWH) and in Vandemark et al. (2016); Hossan and Jones (2021) (for SST).

In summary, sigma$_0$ decreases with increasing incidence angle and wind speed, with quasi-specular scattering dominating at low incidence angles. The rate of decrease in sigma$_0$ with incidence angle is less pronounced at higher wind speeds. Ka-band sigma$_0$ is also more sensitive to Significant Wave Height (SWH) than Ku-band, although this sensitivity diminishes at higher wind speeds and for incidence angles greater than 9°. Additionally, Ka-band sigma$_0$ exhibits greater sensitivity to SST compared to Ku-band.

It is important to note that, as the objective of this paper is not to investigate the fine-scale properties of $sigma_0$, its dependency on SWH and SST is neglected in the following analysis.

c. Correction of the angular dependency

Before delving into the impact of precipitation on KaRin's $sigma_0$, it is essential to correct for geometric effects caused by variations in the incidence angle across the altimeter swath. This ensures that $sigma_0$ amplitude remains consistent throughout the swath, preventing its natural decrease with increasing incidence angle from being misinterpreted as attenuation caused by surface or atmospheric effects.

To achieve this, an angular correction has been defined based on the results presented in Hossan and Jones (2021), which quantifies the dependency of Ka-band $sigma_0$ of the precipitation radars (PR) on-board the Global Precipitation Mission to the incidence angle, wind amplitudes and directions (upwind, downwind and crosswind). For the sake of simplification, a simplified version of this approach is established, depending only on the incidence angle and the magnitude of the wind speed.

A more direct approach could have been used, empirically fitting the incidence angle and wind speed dependency of KaRin $sigma_0$. However, successfully applying the Hossan's method developed for KaPR to Karin demonstrates the good behaviour of KaRin compared to KaPR and participates to the validation of the $sigma_0$.

Hossan's approach involves modeling $sigma_0$ using a Fourier series expansion that captures both isotropic and directional dependencies. Specifically, $sigma_0$ is expressed as a combination of three coefficients, A_0, A_1, and A_2 which capture at different levels of magnitude the impact of wind speed, wind direction and incidence angle on $sigma_0$.

The coefficients are provided for the 25 incidence angles corresponding to the common angles between the Ku- and Ka-band PR. These incidence angles range from approximately 0° to 18°, with a sampling interval of about 0.75°. Hossan examined the variation of $sigma_0$ for wind speeds (ws_{Hossan}) between 2 m/s and 20 m/s by step of 1 m/s.

The first objective is to refine the sampling resolution of the relationship established by Hossan, the sampling of KaRin being finer between -5° and +5°. To achieve this, a second-degree polynomial is fitted to the relationship between $sigma_0$ and the incidence angle of KaPR, for each wind speed

ws_{Hossan} and for the three wind directions.

$$\begin{aligned} {\sigma_0}^{dir}(\theta, ws_{Hossan}) = {a_0}^{dir}(ws_{Hossan}) + \\ {a_1}^{dir}(ws_{Hossan})\theta + \\ {a_2}^{dir}(ws_{Hossan})\theta^2 \end{aligned} \tag{5}$$
$$\text{with } dir \in \{upwind, downwind, crosswind\}$$

The sigma$_0$ value is then calculated for KaRIn theoretical incidence angles (θ_{th}) at each wind speed by averaging the values obtained for the three wind directions. A nadir value is also computed for each wind speed using the same averaging method.

$$\sigma_0(\theta_{th}, ws_{Hossan}) = \frac{\sum_{dir} {\sigma_0}^{dir}(\theta_{th}, ws_{Hossan})}{3} \tag{6}$$
$$\text{for } dir \in \{upwind, downwind, crosswind\}$$

$$\sigma_{0\text{nadir}}(ws_{Hossan}) = \frac{\sum_{dir} {a_0}^{dir}(ws_{Hossan})}{3} \tag{7}$$
$$\text{for } dir \in \{upwind, downwind, crosswind\}$$

The angular correction for KaRIn incidence angles at each wind speed is determined by the difference between the incidence-angle-dependent average value and the nadir value.

$$\begin{aligned} angular\_correction\_LUT(\theta_{th}, ws_{Hossan}) = \\ \sigma_{0\text{nadir}}(ws_{Hossan}) - \\ \sigma_0(\theta_{th}, ws_{Hossan}) \end{aligned} \tag{8}$$

In practice, a two-dimensional look-up table (LUT) is defined with the 35 positive theoretical KaRIn incidence angles, increasing along the rows from 0° to 4.93° in steps of 0.145°. Wind speed increases along the columns from 2 m/s to 20 m/s in steps of 1 m/s, with correction values provided for each grid cell. The actual correction for a given wind speed (ws) and incidence angle (θ) is computed using bilinear interpolation of the LUT.

For each KaRIn observation, the incidence angle θ_{Karin} is derived from the cross-track distance and the altitude provided in Level-2 products, assuming a round Earth model. Wind speed

amplitude is computed from the model wind speed components in the u and v directions, which are also included in the products. The model wind speed (ws_{model}) is preferred over KaRIn wind speed, as it is not affected by atmospheric attenuation and is consistently available. If the amplitude exceeds the LUT range, the values are constrained to the extreme limits of 2 m/s or 20 m/s.

Finally, the angular corrected sigma$_0$ is computed adding the correction (computed for the absolute value of θ_{Karin}) to the initial sigma$_0$.

$$\begin{aligned} \sigma_{0\text{angular\_corrected}}(\theta_{Karin}, w) = \\ \sigma_0(\theta_{Karin}, ws) + \\ angular\_correction\_LUT(|\theta_{Karin}|, ws_{model}) \end{aligned} \tag{9}$$

Figure 2 presents the statistical variation of Ka-band sigma$_0$ as a function of incidence angle and wind speed from different sources. The dashed lines represent the variation of sigma$_0$ for KaPR (from Hossan 2021, fitted and averaged across the three wind directions), the dotted lines show the initial uncorrected KaRIn sigma$_0$, and the solid lines display the angular-corrected KaRIn sigma$_0$.

For KaRIn, the statistics are derived from valid SWOT observations during January 2024. Sigma$_0$ values, both corrected and uncorrected, are averaged according to the incidence angles (ranging from 0.6° to 4.5°) and binned by 1 m/s increments of model wind speed. At higher wind speeds (approximately 12 m/s and above), not all incidence angles are represented, as no valid sigma$_0$ values are observed at the swath edges (near and far). The shaded areas around the average values for wind speeds of 2 m/s, 8 m/s, and 16 m/s represent the ± standard deviation for each incidence angle bin.

The decrease in KaRIn sigma$_0$ with incidence angle closely aligns with the decrease observed for KaPR sigma$_0$. As a result, the angular correction applied to KaRIn demonstrates strong performance for wind speeds between 4 m/s and 14 m/s. A minor positive trend is observed at 4 m/s, with a magnitude of approximately -0.4 dB over the incidence angle range, negligible compared to the -1.3 dB observed in the uncorrected sigma$_0$. The correction is slightly underestimated for wind speeds of 2 m/s, although the overall decrease (-3.15 dB across the swath) is significantly reduced to -0.83 dB in the angular-corrected sigma$_0$.

At 16 m/s, the uncorrected sigma$_0$ decreases by -0.45 dB before exhibiting a slight increase at the swath's far edge, whereas the angular-corrected sigma$_0$ remains stable up to approximately 4°

and subsequently increases by -0.2 dB at 4.3°. For wind speeds of 20 m/s, the incidence angle has minimal impact on uncorrected $sigma_0$ (-0.25 dB), with a slight increase of +0.35 dB at the far edge. The corrected $sigma_0$ is marginally more stable up to 3.6°, after which it follows the same +0.35 dB increase up to 4°.

Since wind speeds below 2 m/s and above 16 m/s account for only 1 % of the valid observations, as illustrated in Figure 3, it can be concluded that the decrease in KaRIn $sigma_0$ with incidence angle is comparable to KaPR for the majority of valid observations. The drop-off is effectively corrected using the methods proposed by Hossan and Jones (2021).

In order to complete the validation of KaRIn $sigma_0$ characteristics, the variation of angular-corrected $sigma_0$ with wind speed is compared to KaPR $sigma_0$ (extracted at nadir from Hossan and Jones (2021)) and to SARAL/AltiKa nadir measurements in Figure 4. The statistics are computed over January 2024, considering only valid observations for KaRIn and SARAL (see Prandi et al. (2015) for the definition of valid AltiKa observations). The shaded gray area around KaRIn $sigma_0$ represents the ± standard deviation around the mean.

Systematic biases are observed between the three instruments. These biases have been corrected for GPM KaPR and SARAL to align with KaRIn $sigma_0$ at a wind speed of 7.5 m/s, corresponding to the global median (see Figure 3). KaRIn $sigma_0$ exceeds the values measured by the other two instruments by +3.3 dB relative to SARAL and +2.3 dB relative to GPM KaPR. Between 3 m/s and 13 m/s (approximately 87 % of the data), the three instruments exhibit similar behavior. At 3 m/s, GPM KaPR and SARAL $sigma_0$ are closely aligned, with KaRIn $sigma_0$ exceeding them by approximately 0.5 dB, within the standard deviation of KaRIn $sigma_0$ at this wind speed (0.9 dB). At 2 m/s, KaRIn and SARAL $sigma_0$ are nearly identical, while GPM KaPR $sigma_0$ is approximately 2 dB lower.

For wind speeds exceeding 13 m/s (around 7 % of the data), GPM KaPR and SARAL $sigma_0$ continue to show similar trends, whereas KaRIn $sigma_0$ displays a stronger, quasi-linear response. The discrepancy between KaRIn and the other instruments increases with wind speed, ranging from -0.5 dB at 13 m/s to -0.9 dB at 16 m/s (the standard deviation of KaRIn $sigma_0$ around 0.6 dB at these wind speeds).

In conclusion, the angular dependency of KaRIn $sigma_0$ closely mirrors that of GPM KaPR and can be effectively corrected. On average, KaRIn $sigma_0$ is 2 dB to 3 dB higher than GPM KaPR and

SARAL sigma$_0$, with a similar wind speed dependency. However, at wind speeds above 13 m/s, KaRIn sigma$_0$ demonstrates a slightly stronger response compared to the other two instruments.

5. Estimating the atmospheric attenuation due to rain and the rainfall rate from KaRin sigma$_0$

To address the challenges associated with identifying KaRIn σ_0 attenuation events caused by precipitation, two complementary approaches were developed. The first approach defines attenuation based on variations in KaRIn σ_0 and establishes a threshold beyond which sea surface height measurements become unreliable. The second approach estimates rainfall rates directly from KaRIn σ_0 using a machine learning method applied to collocations between the SWOT mission and the NEXRAD precipitation radar network. For comparison and validation purposes, an additional rainfall rate estimate is derived directly from attenuation using a Marshall-Palmer type relationship, as recommended by the International Telecommunication Union (ITU). The following sections describe the methodologies employed in these different approaches.

a. Definitions and methods

1) Atmospheric attenuation due to rain

The attenuation is derived from the difference between a smooth version of σ_0 (the background) and the original, unaltered angular-corrected σ_0, consequently isolating the events where the σ_0 is impacted by smaller scale variations. The scale of the small variations is thus determined by the scale of the smoothed version.

In Picard (2021), the background was determined using a median filter applied along-track to σ_0, depending on two parameters: the sizes of two sliding windows, the first for removing km-scale variations and a second with a size of 30 km, defining the smoothed version of σ_0.

We will use here a simplified of this approach based only on the large-scale part: $\widetilde{\sigma_0}^{median}$ involves a median filter applied along-track over a sliding window:

$$\widetilde{\sigma_{0_i}}^{median} = \text{median}\left(\{\sigma_{0_{i+k}} \mid k \in [-W/2, W/2]\}\right) \tag{10}$$

where i represents the current grid cell, and k corresponds to the indices of the grid cells within the same line, inside a window of size W centered at i.

Then the attenuation is defined as:

$$\text{att\_sig0} = \widetilde{\sigma_0}^{median} - \sigma_{0_{\text{angular\_corrected}}} \tag{11}$$

The computation of the attenuation is illustrated in Figure 5, which presents a cross-section along pixel #41 under different atmospheric and surface conditions. The black solid line represents the KaRIn σ_0 in dB, corrected for angular dependency. The orange, green, red, and violet solid lines correspond to different window sizes for the median filter, specifically 200 km, 400 km, 800 km, and 1200 km.

Panel (a) depicts the segment highlighted in red in Figure 1, panel (b), corresponding to track 132 of cycle 16. The shaded areas indicate regions where the attenuation, as defined by Eq. 11, exceeds 0 dB when computed with a 800 km window size or 1.5 dB when computed with a 1200 km window size. The observed strong attenuation events, with values reaching approximately 60 dB, can be unambiguously attributed to precipitation cells. The different smoothing window sizes yield consistent results in detecting these precipitation-induced attenuation patterns.

Panels (b) and (c), extracted from track 134 of cycle 16, illustrate more complex situations where attenuation patterns are less straightforward to interpret. In panel (b), two significant attenuation events, centered around latitudes 7.5° and 8.5°, reach values of approximately 8 dB, a magnitude consistent with precipitation-induced attenuation. In contrast, the variations observed between latitudes 6.5° and 7.5°, which exhibit attenuation values below 1 dB, are more ambiguous. Whether these small-scale fluctuations originate from the surface or from atmospheric effects remains uncertain. The analysis of different window sizes highlights the limitations associated with background subtraction: when computed with a 1200 km window size, the background σ_0 captures very large-scale variations and leads to a slight overestimation of attenuation by approximately 0.5 dB. On the other hand, the 400 km window size is influenced by the two precipitation events described earlier, resulting in an underestimation of the second attenuation event by about 0.5 dB.

A similar effect is observed in panel (c), which follows the geographical continuity of panel (b). Here, the impact of selecting a small window size is particularly evident. When the attenuation

region associated with precipitation extends over a spatial scale larger than the filtering window, the method fails to properly capture the full extent of the event, leading to an underestimation of attenuation, in this example by approximately 8 dB. Additionally, this panel highlights a case where background subtraction using 400 km and 800 km window sizes introduces a false detection of attenuation: the variation of KaRIn σ_0 in the neighborhood of this area, lead to a spurious attenuation signal of about 1 dB, despite the likely absence of precipitation.

These results underscore the critical role of window size selection in the accurate detection of precipitation-induced attenuation. While larger windows (e.g., 1200 km) effectively capture broad-scale variations, they may overestimate attenuation in areas where non-meteorological fluctuations occur. Conversely, smaller windows (e.g., 200 km) risk underestimating the magnitude of attenuation when precipitation cells extend beyond the filtering scale. Intermediate window sizes (e.g., 400 km or 800 km) can be sensitive to surrounding variations in KaRIn σ_0, potentially leading to false detections. These findings highlight the trade-off between spatial resolution and attenuation estimation accuracy, a key aspect to consider when analyzing KaRIn Ka-band backscatter measurements in the presence of precipitation. Ultimately, a window size of 1200 km was selected, combined with an additional filtering step that removes attenuation below 1.5 dB. This threshold corresponds approximately to a rainfall rate of 1 mm/hr. The subsequent analysis of the percentage of observations flagged as rain-affected confirms the robustness of this choice.

2) Rainfall rate computed from attenuation using ITU model

The ITU-R P.838-3 recommendation International Telecommunication Union Radiocommunication Sector (ITU-R) (2005) provides a standardized model for estimating specific rain attenuation in radiowave propagation. It defines a power-law relationship between attenuation γ_R (dB/km) and rainfall rate R (mm/h), with frequency-dependent coefficients derived from electromagnetic scattering calculations:

$$\gamma_R = k R^{\alpha} \tag{12}$$

where the coefficients k and α are functions of the radar frequency f (GHz). Based on Equations (4) and (5) in International Telecommunication Union Radiocommunication Sector (ITU-R) (2005), and assuming a negligible angular dependency within the SWOT narrow swath, these coefficients

are computed as:

$$k = (k_H + k_V)/2 \tag{13}$$

$$\alpha = (k_H \alpha_H + k_V \alpha_V)/2k \tag{14}$$

where the values $k_H = 0.3789$, $\alpha_H = 0.8890$, $k_V = 0.3633$ and $\alpha_V = 0.8621$ are taken from Table 5 of International Telecommunication Union Radiocommunication Sector (ITU-R) (2005) for $f = 37$ GHz, corresponding to KaRIn's Ka-band frequency. To account for the path reduction effect in rain-induced attenuation, the ITU-R P.530-18 recommendation for propagation data and prediction methods International Telecommunication Union Radiocommunication Sector (ITU-R) (2022) introduces an updated path reduction factor r, defined as:

$$r = \frac{1}{0.477 \left(L_p^{0.633}\right) R_p^{0.073} a f^{0.123} - 10.579 \left[1 - \exp(-0.024 L_p)\right]} \tag{15}$$

where L_p represents the rain cell height (km). The relationship between the rainfall rate through γ_R and the attenuation (A_p in dB) is then expressed as:

$$A_p = \gamma_R r L_p \tag{16}$$

To retrieve the rainfall rate from the measured attenuation, a power-law relationship of the form $R = a A_p^b$ is fitted based on the computed relationship in Eq. 16. This fitting is performed over attenuation values ranging from 0 dB to 100 dB (in 1 dB steps) and rain cell heights varying from 0 km to 6 km (in 500 m steps).

The rainfall rate is then estimated from the 2D lookup table using bilinear interpolation, with the KaRIn attenuation values, computed via Eq. 11, and the rain cell height as input variables:

$$R_{ITU} = LUT(\text{att\_sig0}^{median}, \text{height}) \tag{17}$$

The latter is determined from a static gridded map (2° latitude × 1.5° longitude resolution) made available by the ITU, as described in the ITU-R P.839-4 recommendation for the Rain Height Model for Prediction Methods International Telecommunication Union Radiocommunication Sector (ITU-R) (2013).

Figure 6 illustrates the accuracy with which the relationship between attenuation (dB) and rainfall rate (mm/hr), as derived from the ITU-R attenuation model, is captured by the methodology used to construct the lookup table. The solid lines represent the theoretical relationship defined in Eq. 16, while the cross markers indicate the best-fit approximation using a power-law function. The results are shown for different rain cell heights ranging from 1 km to 5 km.

As described in the review of rain signal attenuation models performed by Alozie et al. in 2022 Alozie et al. (2022), the ITU rain attenuation model presents several limitations in accurately describing the relationship between rainfall rate and attenuation. Firstly, it primarily accounts for rain-induced attenuation, neglecting other meteorological effects such as hail, snow, and atmospheric turbulence, which can introduce additional errors. Secondly, the model has been shown to exhibit poor correlation with experimental data, particularly in tropical regions, where raindrop size distributions are highly variable and inhomogeneous. Finally, its applicability is limited for high-intensity rainfall scenarios, as errors can reach up to 10 % when applied outside its intended frequency and rainfall rate ranges.

As noted by Alozie et al., a machine learning-based approach could help overcome the limitations of statistical models such as the one proposed by the ITU. The following section provides a detailed description of this approach.

3) A random forest approach for the retrieval of rain from KaRIn σ_0

The methodology for estimating rainfall from KaRIn backscatter coefficients involves colocating KaRIn σ_0 with precipitation measurements from the NEXRAD radar network. It inherits from a previous study performed by Colin and Husson in 2021 for Sentinel-1 Colin and Husson (2024). This study presents a machine learning approach using Multi-Task Generative Adversarial Networks (MT-GANs) to estimate precipitation rates from C-band Synthetic Aperture Radar (SAR) data at a 200 m spatial resolution. By leveraging co-located Sentinel-1 SAR and NEXRAD weather radar observations, the model improves on previous methods by addressing issues such as collocation misalignment and the scarcity of high-wind rainfall examples. The model undergoes extensive training on 29,369 Sentinel-1 wide-swath observations, with a focus on reducing false positives in heavy wind conditions and enhancing rainfall detection performance. Results demonstrate higher precision and generalization capability compared to previous SAR-based rainfall estimation

techniques, making this method a promising candidate for improving high-resolution satellite-based precipitation monitoring.

A simplified approach is applied here as the first attempt to retrieve rainfall in the specific configuration of the 2D Ka-band backscatter coefficient.

The NEXRAD system provides high-resolution precipitation data, including Digital Precipitation Rate (DPR) and Hybrid Hydrometeor Classification (HHC), with a range resolution of 250 m and an azimuthal resolution of 1°. To ensure consistency, only observations within 175 km of a NEXRAD station are retained, as the minimum elevation angle of 0.5° causes increasing beam height with distance. When multiple NEXRAD observations overlap with a SWOT track, all are retained. The delay between two successive observations from NEXRAD is 6 min. Thus, each collocation will have a delay of, at most, half of the time delta between two observations i.e. 3 min.

SWOT tracks are segmented into 32-line segments along the track direction, corresponding to approximately 12 seconds of observation time. Each of these segments is further divided into left and right portions, creating subpatches with a 32×32 grid structure. However, certain conditions can result in invalid values within these subpatches. These include the presence of land, the edges of the SWOT observation swath, or limitations imposed by NEXRAD data, which is constrained to a maximum range of 175 km. In all these cases, the affected data points are marked as NaN (Not a Number).

An example of a NEXRAD-collocated measurement on the SWOT grid is presented in Figure 1, panel d, depicting the rainfall rate observed by the KBYX station. This particular case was selected due to its strong correlation between the SWOT-derived signal and the corresponding NEXRAD weather radar observations. While this instance demonstrates a high level of consistency, other collocations may exhibit greater discrepancies due to factors such as spatial variability and differences in measurement sensitivity. Nevertheless, the application of a maximum temporal offset of 3 minutes helps mitigate inconsistencies by minimizing temporal misalignment between the two datasets.

The features for the retrieval algorithms consists of a vector of nine parameters. To convert the dataset from subpatches (2D data) to an array-based dataset (1D data), two approaches are employed:

- Pixel-wise data (parameters 1 to 3) directly utilize per-pixel values.

- Subpatch-wise metrics (parameters 4 to 8) summarize statistical properties over the entire subpatch.

The final parameter (parameter 9) is included as a control variable to monitor potential overfitting. The full list of features is as follows:

1. KaRIn backscatter coefficient (σ_0, linear version)
2. Incidence angle
3. Wind speed from ERA5
4. Mean of σ_0
5. Standard deviation of σ_0
6. Skewness of σ_0
7. Kurtosis of σ_0
8. Polarization (0 or 1)
9. Line index

The development of this approach is complex and began during the early stages of mission validation, at a time when the conversion of σ_0 to decibel units and the angular correction were not yet available. Consequently, the input features include the linear σ_0 as well as the raw incidence angle. Future iterations of the algorithm will take advantage of the most recent processing developments, including calibrated σ_0 values and corrected incidence angles, thereby improving both detection accuracy and robustness.

The dataset is divided into training, validation, and test subsets while ensuring spatial consistency to prevent data leakage. To address the strong imbalance caused by the predominance of rain-free pixels, only 1 % of such cases are retained in the dataset.

For model development, an XGBoost-based random forest regression is trained on approximately $\sim 200,000$ samples, with an additional $\sim 50,000$ samples allocated for validation and testing.

Hyperparameter tuning is performed using a randomized search over 10,000 configurations, optimizing the model based on the Pearson Correlation Coefficient (PCC) and the Mean Squared

Error (MSE). The two key performance metrics exhibit a strong inverse correlation, as PCC is maximized while MSE is minimized, with an approximate correlation of -1. This indicates that selecting models based on one of these metrics yields similar results, simplifying the optimization process.

Furthermore, a feature importance analysis using Shapley values Lundberg and Lee (2017) provides insights into the contribution of each feature. The Figure 7 shows the SHAP value (SHapley Additive exPlanations) for each of the nine inputs parameters. As expected, the KaRIn backscatter coefficient (σ_0) has the highest influence on rainfall estimation. In contrast, certain parameters, such as polarization and the line index, appear to have minimal impact, suggesting their potential removal in future iterations of the model. Additionally, the incidence angle exhibits a weak but noticeable effect, with larger incidence angles leading to lower estimated precipitation rates. Higher-order statistical moments of σ_0, such as skewness and kurtosis, contribute little to the model's predictive capacity. These findings indicate that a more streamlined model could be achieved by excluding non-contributory features while maintaining high prediction accuracy.

To further refine the model's predictions, quantile mapping is applied as a post-processing step to correct biases in rainfall estimation: it slightly improves the performances of the retrieval for rainfall rates larger than about 15 mm/hr.

Figure 8 shows a qualitative comparison of KaRIn backscatter coefficient (σ_0) (top row), collocated NEXRAD rainfall rate (middle row), and predicted rainfall rate based on the random forest approach (R_{RF}) (bottom row) under various precipitation conditions (one per column). Qualitative assessment of the results indicates that the model effectively detects rain cells in most cases, although discrepancies remain in the estimated precipitation rates. In particular, for low precipitation intensities (right-most column), the model occasionally fails to detect rainfall. Previous studies suggest that this limitation is especially pronounced for stratiform precipitation, where weak radar backscatter signals may reduce detection sensitivity.

b. Quantitative validation

1) Comparison to NEXRAD in-situ rainfall rates

The rainfall rates retrieved from KaRIn are compared to a subset of the NEXRAD observations used to validate the random forest model. All the observations of actual precipitations by the

weather radars are selected and 10 % of the observations where the rainfall rate is null, leading to a total of observations of about $\sim 380,000$.

Figure 9 presents the mean rainfall rates retrieved from KaRIn σ_0, binned as a function of NEXRAD rainfall rates in 2.5 mm/hr intervals. Two retrieval approaches are shown: the random forest regression (R_{RF}, blue solid line) and the ITU-based model (R_{ITU}, orange solid line). The dashed lines indicate the standard deviation within each bin. The number of observations per bin is plotted on the secondary y-axis (logarithmic scale, gray line), highlighting the sharp decrease in sample size beyond 15 mm/hr—falling below 1,000—which limits statistical robustness for higher rain intensities.

The R_{RF} retrieval shows good agreement with NEXRAD reference values, following the 1:1 line (dashed black) with limited bias over the full range. In contrast, R_{ITU} systematically underestimates rainfall, with biases increasing with intensity: approximately 2 mm/hr at 10 mm/hr, 10 mm/hr at 30 mm/hr, and up to 20 mm/hr at 50 mm/hr. This underestimation may arise from assumptions in the ITU attenuation–rain rate relationship (e.g., the Marshall–Palmer parameterization), uncertainties in rain cell vertical extent, or a possible underestimation of the KaRIn-derived atmospheric attenuation.

The spread in retrievals, as quantified by the standard deviation (dashed line), is notably different between the two methods. While R_{ITU} exhibits lower variability (ranging from 1.5 mm/hr to 20 mm/hr), R_{RF} shows larger dispersion (2.2 mm/hr to 48 mm/hr), possibly reflecting its sensitivity to noisy or unmodeled inputs despite better average accuracy.

Figure 10 shows the confusion matrices comparing the classification provided by R_{RF} (panel a) and R_{ITU} (panel b) to the classification provided by NEXRAD stations. Based on the results shown below on the thresholds of rainfall rate that prevent the measurement of SSH by the KaRIn, the classification distinguishes the following cases: no rain (rainfall rate below 1 mm/hr), light rainfall rate with no impact on SSH (rainfall rate between 1 mm/hr to 5 mm/hr), rainfall rate with potential impact on SSH (depending on the validation criteria used, for rainfall rate between 5 mm/hr and 10 mm/hr), and stronger rainfall rate for which the measurement of SSH is invalid (rainfall rate larger than 10 mm/hr).

Both retrieval approaches based on KaRIn σ_0 demonstrate a strong ability to correctly identify rain-free conditions. The ITU-based method (R_{ITU}) performs slightly better, achieving a correct

classification rate of 94 %, compared to 91 %. This improved performance is primarily due to a lower rate of confusion for R_{ITU} with light rainfall events below 5 mm/hr (5 % against 9 % for R_{RF}).

The sensitivity is smaller for light rain below 5 mm/hr with a rate of about 32 % for R_{ITU} and 44 % for R_{RF}. But since most of those cases are confused with no rain cases, it means that the retrievals are still capable of distinguish cases where the SSH is not impacted by rain with a rate of more than 90 % for both approaches.

The sensitivity for cases where the rain fall may have an impact of SSH is poor for both approaches. It is retrieved in the correct class on about 17% of the cases, confused with a rate of more than 6 0% with cases where the rainfall rate is smaller than 5 mm/hr for both approaches.

The cases where the rainfall rate is above 10 mm/hr and thus lead to invalid measurements of the SSH are detected with a rate below 50 %, slightly better with the R_{RF} solution (about 42 %) than with R_{ITU} (about 33 %). More than 35 % of those cases are confused with rainfall rate bellow 5 mm/hr which could be problematic for a good labeling of the invalid SSH measurements caused by rain.

These results should be compared to the confusion matrix constructed from two distinct NEXRAD stations observing the same precipitation events (Figure 10(c)). This comparison highlights the intrinsic difficulty in accurately detecting precipitation, even with ground-based radar systems. Notably, high-intensity rainfall events—those likely to invalidate SSH retrievals—are jointly detected by both stations in only about 30 % of the cases. Conversely, approximately 28 % of these high-rainfall events are misclassified by at least one station as either light rain or no rain at all.

The validation of KaRIn-derived rainfall rates against NEXRAD ground radar observations highlights both the strengths and limitations of the two retrieval approaches. The random forest model (R_{RF}) provides accurate mean estimates and improved detection of high rainfall events, but it may inherit misclassification errors present in the NEXRAD training data. In contrast, the ITU-based physical model (R_{ITU}) offers a consistent and independent retrieval method, less sensitive to local observation errors. However, it systematically underestimates rainfall intensities, especially under heavy precipitation conditions. These findings underline the robustness of the ITU approach in terms of independence from ground radar datasets, but also its limitations in intensity

retrieval, while the random forest model yields better agreement with reference data, at the expense of reproducing NEXRAD's own observational uncertainties. To assess the generalizability of these results beyond the Gulf of Mexico region, a complementary comparison with satellite-based rainfall products at global scale is necessary.

2) Global comparison to gridded satellite-based rainfall rates

Figure 11 presents a comparison of the geographical distribution of monthly mean rainfall rates for January 2024, averaged on a $1^\circ \times 1^\circ$ grid. Three datasets are shown: panel (a) displays estimates from the random forest retrieval (R_{RF}), panel (b) from the ITU-based model (R_{ITU}), and panel (c) from the Special Sensor Microwave Imager/Sounder (SSMIS) aboard the Defense Meteorological Satellite Program (DMSP) F18 platform. The SSMIS rainfall estimates are produced by Remote Sensing Systems Wentz et al. (2012) and were regridded from their original $0.25^\circ \times 0.25^\circ$ resolution to match the $1^\circ \times 1^\circ$ grid used for the KaRIn-based retrievals.

With a swath width of approximately 1700 km—nearly ten times larger than that of KaRIn—SSMIS offers broader coverage, resulting in smoother spatial patterns and less speckle in the rainfall maps. Despite this resolution difference, the zonal structure of rainfall is broadly consistent across datasets. All three maps highlight enhanced precipitation over the Intertropical Convergence Zone (ITCZ), dominated by deep convection, and over the mid-latitudes, where synoptic-scale systems and frontal lifting produce stratiform precipitation.

While R_{RF} and R_{ITU} show similar structures in the ITCZ, notable discrepancies emerge at higher latitudes. In particular, R_{ITU} captures a greater number of low-intensity rainfall occurrences in the southern mid-latitudes, and to a lesser extent in the north—features that are also visible in the SSMIS data but are largely absent in the R_{RF} estimates. Conversely, R_{RF} appears more robust to surface ice contamination, which leads to spurious rainfall detection in R_{ITU}, notably in the Sea of Okhotsk, east of the Kamchatka Peninsula.

Figure 12 shows the zonal mean rainfall rate for January 2024, computed from the gridded products presented in Figure 11. In addition to the KaRIn-based estimates from the random forest model (R_{RF}, solid blue line) and the ITU-based model (R_{ITU}, dashed orange line), the figure includes rainfall rates derived from the Special Sensor Microwave Imager/Sounder (SSMIS, solid black line), the Advanced Microwave Scanning Radiometer-2 (AMSR-2, dashed black line), and

the European Centre for Medium-Range Weather Forecasts (ECMWF) reanalysis data interpolated in the SWOT product (solid green line).

Across the Intertropical Convergence Zone (ITCZ), where precipitation rates peak, the various products generally converge to similar values, with the exception of R_{RF}, which displays rainfall intensities nearly twice as large as the other estimates (0.6 mm/hr versus approximately 0.35 mm/hr). A similar overestimation by R_{RF} is observed around 10°S. These anomalies may reflect a systematic overestimation by the random forest model or, alternatively, the enhanced sensitivity of the high-resolution KaRIn observations to intense, small-scale convective events, which tend to be smoothed out in coarser-resolution microwave radiometer data such as SSMIS and AMSR-2 (spatial resolution ¿20 km, compared to 2 km for KaRIn). Importantly, this explanation is not incompatible with the fact that the R_{ITU} retrieval underestimates high-intensity rainfall, as shown in previous analyses. The present comparison, based solely on gridded products, does not allow us to discriminate between these two hypotheses; future work based on along-track products will provide further insight.

Consistent with the spatial maps, the zonal mean also highlights a systematic underestimation of mid-latitude precipitation by R_{RF} relative to other datasets. A pronounced overestimation is observed near 58°N, corresponding to the Sea of Okhotsk, where surface ice contamination induces strong biases in the R_{RF} retrieval. However, this impact is generally more limited than in the R_{ITU} solution, which systematically interprets low backscatter associated with ice as enhanced attenuation due to rain. In contrast, the random forest model, which uses multiple auxiliary parameters, appears more robust to this confusion.

To mitigate ice-related artifacts in the R_{ITU} retrieval, a filtering criterion was applied: for latitudes poleward of +55° or -60°, rainfall rates are set to zero when total attenuation is less than 1 dB. As shown by the solid orange line, this simple filter significantly improves consistency with the other datasets, especially in high-latitude regions.

c. Characterization of the impact of rain on SSH and discussion on SWOT mission requirements

Beyond the retrieval of rainfall rate, two critical objectives for the SWOT mission—and by extension, for future swath altimetry missions—are: (1) the ability to systematically identify cases where precipitation is responsible for the degradation or invalidity of the sea surface height (SSH)

measurements, and (2) the quantification of the proportion of data loss directly attributable to precipitation.

To address the first objective, all observations affected by a minimum rainfall rate were selected, and the proportion of invalid SSH measurements was computed. The minimum threshold was then progressively increased until nearly all selected observations were classified as invalid.

The results are shown in Figure 13. The two approaches for rainfall rates were used, the random forest approach (blue lines) and the ITU-based model (orange line) and two validity flags were tested, the L2 validity flag (`ssha_karin_2_qual`, dashed lines) and the L3 validity flag (`cvl_flag_val`, solid lines) (see the section a).

The results are presented in Figure 13. Two rainfall rate estimators were used: the ITU-based model (R_{ITU}, orange lines) and the random forest estimator (R_{RF}, blue lines). For each, the percentage of invalid SSH measurements was computed using two distinct validity criteria: the Level-2 quality flag (`ssha_karin_2_qual`, dashed lines) and the Level-3 DUACS-derived validity flag (`cvl_flag_val`, solid lines) (see Section a).

Both rain rate estimators yield consistent results in terms of identifying the minimum rain rate above which a given proportion of SSH data is flagged as invalid. However, the threshold values differ markedly depending on the validity flag used. When relying on the L2 quality flag, more than 95 % and 98 % of SSH observations are invalid for rainfall rates exceeding approximately 10 mm/hr and 14 mm/hr, respectively. In contrast, when using the L3 validity flag, these thresholds are reduced to about 5 mm/hr and 7 mm/hr.

This twofold reduction highlights the increased sensitivity of the Level-3 editing chain to rain-induced anomalies, in agreement with Dibarboure et al. (2024), which emphasizes the limitations of Level-2 flags in the context of non-Gaussian perturbations such as those caused by intense rain cells. Level-2 quality flags often rely on formal uncertainty estimates derived from theoretical models and may fail to capture visually apparent but statistically irregular anomalies. Conversely, the Level-3 editing process used in the DUACS system applies adaptive, data-driven methods. In particular, two steps in the Level-3 chain are effective in detecting rain-contaminated measurements: (i) comparison of local SSH statistics against expected variability conditioned on significant wave height, and (ii) a local consistency check using Gaussian smoothing over a 20 km window to highlight sharp gradients or outliers in the SSHA field.

As a first step, Figure 14 presents the zonal mean of the percentage of observations for which a non-zero rainfall rate has been detected using the two retrieval approaches (i.e., without applying any minimum threshold on the rain rate) relative to the total number of non-NaN observations. These are compared against the rainfall occurrence derived from the ECMWF rain rate provided in the Level-2 SWOT product (solid green line). The ECMWF-based occurrence is systematically higher, exceeding the estimates from KaRIn-derived methods by approximately 7 % over the Intertropical Convergence Zone (ITCZ) and by 2–4 % over southern latitudes. The KaRIn-based retrievals show good internal consistency, with R_{RF} results plotted in blue and R_{ITU} in orange.

In the Southern Hemisphere, within the latitudinal range where ocean ice is minimal, both retrieval approaches yield similar rain occurrence rates, consistent with previous results obtained using AltiKa data Picard (2021). This confirms the robustness of the methods when applied to Ka-band altimetry.

At mid-latitudes in the Northern Hemisphere, the R_{RF} approach estimates that approximately 8 % of observations are affected by rain, which is about 2 % higher than the R_{ITU} estimate and also greater than the values reported for AltiKa (typically below 5 %). This difference may be attributed to the enhanced ability of the R_{ITU} method to discriminate between rainy and non-rainy scenes at low rain rates, as suggested by the confusion matrices shown in Figure 10.

It is worth noting that the ability of the R_{ITU} approach to discriminate between rain and ocean ice is clearly demonstrated in this figure. In contrast, the R_{RF} retrieval still exhibits spurious detections at high latitudes, as evidenced by anomalously high values just below +60°N and around –70°S.

Using the previously defined rainfall rate thresholds, Figure 15 shows the zonal distribution of the percentage of SSH observations degraded by rain, relative to the total number of non-NaN observations. Two thresholds are tested: 5 mm/hr (solid lines), corresponding to the Level-3 quality flag criterion, and 15 mm/hr (dashed lines), a more conservative threshold associated with the Level-2 flag. These distributions represent the proportion of KaRIn measurements degraded by rain for each latitude band.

For the 5 mm/hr threshold, the percentage of degraded observations peaks over the Intertropical Convergence Zone (ITCZ), reaching approximately 1.8% with the R_{RF} approach and 1.35% with R_{ITU}. This discrepancy is consistent with the previously identified underestimation of rainfall rates by R_{ITU} (Figure 9), supporting the higher reliability of the R_{RF}-based estimates. Outside

the ITCZ, the fraction of rain-degraded measurements falls below 0.5%, except in high-latitude regions affected by misclassification with ocean ice—around +60°N for R_{RF} and south of –60°S for R_{ITU}.

When the more conservative threshold of 15 mm/hr is applied, associated with the Level-2 quality flag, less reliable and likely underestimating rain-related degradation, the percentage of invalid observations decreases substantially. In this case, the proportion of affected data drops to about 0.6% over the ITCZ and becomes negligible beyond 20° latitude.

This analysis also provides valuable insights for future missions in terms of defining a degradation threshold based on radar signal attenuation. As illustrated by the dotted dashed black line in Figure 15, applying a 10 dB attenuation threshold (as defined in Equation 11) reproduces the latitudinal pattern of degraded observations obtained using the 5 mm/hr R_{RF} threshold. This suggests that 10 dB of attenuation can be considered a critical limit above which KaRIn SSH measurements become unreliable.

Finally, building on the 5 mm/hr threshold and the R_{RF} retrieval, Figure 16 displays the global map of data availability in the presence of rain, aggregated on a 1°×1° grid for January 2024. The average global availability reaches 99.6%, with values remaining above 98.5% even across the ITCZ. However, specific regions—particularly in the western tropical Pacific and the central Atlantic—exhibit localized reductions of up to 10%, reflecting the spatial variability of rain-induced signal degradation.

Following this analysis, it is possible to reassess the data availability requirements defined in the SWOT Science Requirements Document SWOT Project Science Team (2018). In this document, Requirement 2.5.4.c (Threshold Science Mission) states that *"rain rates above 3mm/hour severely attenuate the radar signal, making the measurement unfeasible. At any given time, about 7 % of the Earth's surface will experience these rain rates"*. The results presented here provide a more detailed evaluation of this assertion. First, the zonal distribution of rain occurrence (Figure 14) provides a more detailed characterization of rain-induced contamination compared to global statistics, and confirms that the fraction of observations affected by rain remains generally below 8 %. Furthermore, we identified 5 mm/hr as a more accurate threshold above which SSH observations begin to show significant degradation. For this refined threshold, the percentage of

degraded observations is consistently below 2.5 %, suggesting that the 3 mm/hr threshold cited in the requirements may be slightly conservative when considering actual SSH validity.

Requirements 2.7.4 and 2.8.9 of the SWOT Science Requirements Document more explicitly address the impact of precipitation on measurement validity. They state that *"SWOT shall provide flagging of height postings affected by rain with 68 % accuracy of the rain (More than 68 % of rain-contaminated data must be correctly flagged)"* and *"SWOT shall provide flagging of height postings affected by rain in both the pass-by-pass and global data, with 68 % accuracy of the rain flag. Rain cells significantly distort Ka-band radar measurements due to signal attenuation"*, respectively SWOT Project Science Team (2018).

Based solely on the confusion matrices comparing KaRIn-derived detection to NEXRAD ground observations (Figure 10), only approximately 40 % of rainfall events with rates above 5 mm/hr are correctly identified. However, this discrepancy must be interpreted with caution, as uncertainties in the NEXRAD measurements themselves can be significant. Despite this, the close agreement between the zonal averages of rainfall rates derived from KaRIn observations and those from passive microwave sensors such as SSM/I(S) and AMSR-2 suggests that both retrieval approaches—R_{RF} and R_{ITU}—provide sufficient skill to discriminate rainfall events above or below the critical threshold of 5 mm/hr.

Moreover, given that more than 95 % of the SSH observations associated with rainfall rates exceeding 5 mm/hr are flagged as invalid by the Level-3 quality flag, and considering that such high rain rates occur in less than 0.01 % of the valid dataset, it is highly likely that either of the proposed detection approaches is capable of meeting the flagging performance required by the mission.

6. Conclusions

This study provides a comprehensive assessment of the sensitivity of the Ka-band swath altimeter KaRIn onboard the SWOT mission to precipitation, starting with an in-depth characterization of the normalized radar backscatter coefficient σ_0. Since KaRIn σ_0 is provided in linear units and may include negative values due to atmospheric attenuation, a novel three-regime conversion strategy to decibels was introduced to ensure numerical stability and dynamic range preservation. This was followed by a correction of the angular dependence of σ_0, which stems from the varying

incidence angles across the SWOT swath. The proposed correction approach was derived from a parametric model originally developed for the Ka-band Precipitation Radar (KaPR) on board GPM, using polynomial fits to represent the angular response under varying wind conditions. The corrected KaRIn σ_0 profiles were then validated against those of KaPR and the nadir-viewing SARAL/AltiKa altimeter. Across wind speeds ranging from 3 to 13 m/s—covering more than 85 % of the global ocean observations—KaRIn σ_0 showed consistent angular trends and wind dependencies, with systematic biases of +2.3 dB relative to KaPR and +3.3 dB relative to AltiKa. These results confirm the strong coherence of KaRIn radiometric behavior with heritage Ka-band sensors, while highlighting its enhanced sensitivity to surface roughness, especially at high wind speeds and incidence angles. This preliminary cross-instrument validation is essential for establishing a robust baseline from which precipitation-induced anomalies can be isolated and interpreted.

Building on this radiometric foundation, two complementary algorithms were developed to estimate rainfall rates directly from KaRIn σ_0 observations. The first relies on a physical model that converts attenuation into rain rate using the ITU-R power-law relation, assuming constant incidence geometry and exploiting a reference σ_0 under clear-sky conditions. The second is a supervised machine learning method based on a random forest classifier, trained using coincident observations from NEXRAD precipitation radars. This approach allows for a flexible mapping of σ_0 anomalies into rain rates, while accounting for non-linear effects and contextual dependencies. The comparison of both methods demonstrates their complementarity: while the physical model is more robust in low to moderate rainfall regimes, the random forest approach better captures extreme events and spatial gradients.

The results confirm that rainfall rates exceeding 5 mm/hr (or an attenuation of 10 dB) significantly degrade SWOT sea surface height (SSH) measurements, consistent with mission requirements, and provide a robust empirical basis for the design of rain flagging algorithms in future Ka-band altimetry missions. Notably, more than 95 % of SSH observations associated with rain rates above this threshold are correctly identified as invalid by the Level-3 editing chain, which is confirmed here to outperform the Level-2 quality flags in filtering out rain-degraded data. The Level-2 indicators are found to be overly permissive in this context. This empirically derived 5 mm/hr threshold thus refines the initial SWOT mission specification of 3 mm/hr and supports the

implementation of adaptive data quality screening procedures that reflect the actual radiometric sensitivity to precipitation.

The primary perspective of this work is to extend the current methodologies to the 250-m KaRIn product. The availability of this product opens the possibility to approach the observational framework used by Colin and Husson (2024) in their study of rain detection using Sentinel-1 SAR data, which operates at a spatial resolution of approximately 200 m. At this finer resolution, the distinction between wind-induced and rain-induced signatures may be facilitated, as wind and rain typically exhibit markedly different spatial scales and textural properties. In particular, wind-related backscatter tends to vary smoothly over several kilometers, whereas rain cells often produce highly localized and irregular attenuation patterns.

To leverage these spatial frequency differences, future work will consider incorporating texture-sensitive detection strategies. As demonstrated in the Sentinel-1 context, convolutional neural networks (CNNs) are particularly well suited for this purpose. CNNs can exploit spatial patterns within local neighborhoods and are inherently capable of distinguishing structural features such as rain cells from more homogeneous wind signatures. Consequently, a transition from the random forest classifier used in the present study to a convolutional deep learning architecture will be explored, with the aim of enhancing rain detection accuracy at high spatial resolution.

On the feature selection side, the volumetric coherence—used operationally to retrieve significant wave height (SWH)—has been identified as highly sensitive to precipitation-induced signal decorrelation. As such, it will be tested as a new input variable for future machine learning models to exploit its sensitivity to rain-contaminated returns.

Regarding the training strategy, improvements will focus on refining the collocation between KaRIn observations and ground-based NEXRAD radar estimates. As current results suggest that the correlation between the two datasets can be limited due to spatial and temporal mismatches, stricter collocation criteria will be applied to improve the quality and consistency of the training dataset. This refinement aims to enhance the physical representativity of the supervised learning framework and reduce residual uncertainties in the retrieval performance.

Beyond their relevance to SWOT, these findings directly inform the preparation of next-generation Ka-band altimetric missions. The Sentinel-3 Next Generation (S3-NG) mission, currently under development, will integrate a swath altimeter operating at Ka-band, with enhanced temporal and

spatial coverage. The algorithms and methodologies presented here—particularly the machine learning-based retrieval trained against high-resolution precipitation radar data—offer a validated framework for onboard or ground-based flagging and correction schemes that can be applied to S3-NG from the early stages of mission calibration.

Furthermore, the ODYSEA mission, planned as a joint CNES–NASA initiative, will explore fine-scale air–sea interactions by measuring ocean surface currents and wind vectors with unprecedented spatial resolution (approximately 5 km) and high temporal revisit. As emphasized by Torres et al. (2023), ODYSEA will rely on Ka-band Doppler scatterometry, a technique particularly sensitive to rain-induced signal contamination. The high fidelity characterization of precipitation-induced attenuation performed in this study provides critical input for the design of ODYSEA's rain filtering algorithms and error modeling. In particular, the demonstrated capability of Ka-band sensors to detect small-scale rain cells and quantify attenuation statistics enhances the mission's ability to disentangle wind and current signals from hydrometeorological noise—crucial for estimating the wind work at the air–sea interface, one of ODYSEA's core objectives.

In summary, the lessons learned from SWOT not only advance our understanding of precipitation effects on swath altimetry but also lay the technical foundation for future missions targeting ocean dynamics and air–sea fluxes at the mesoscale and submesoscale.

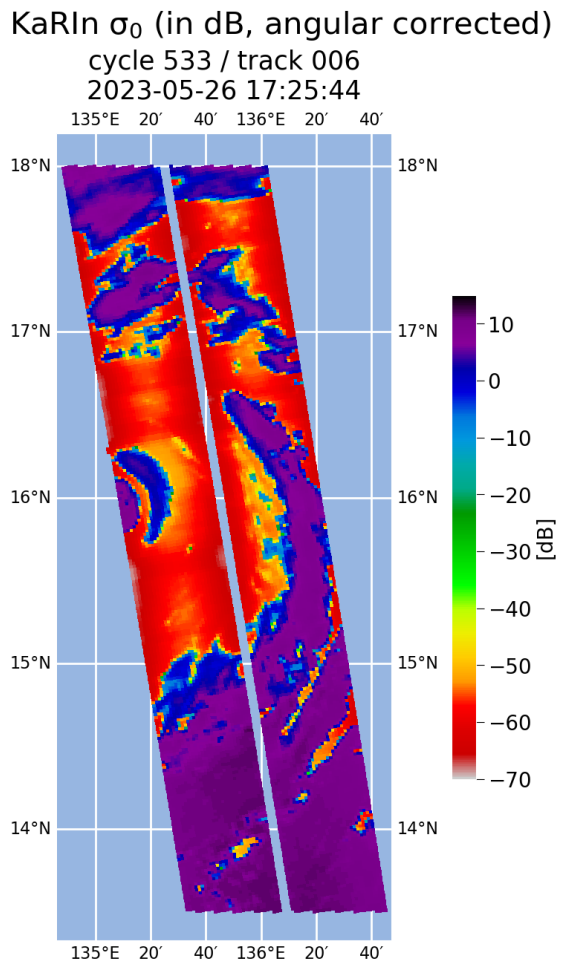
KaRIn σ0 (in dB, angular corrected)
cycle 533 / track 006
2023-05-26 17:25:44
135°E 20′ 40′ 136°E 20′ 40′
18°N
17°N
16°N
15°N
14°N
10
0
−10
−20
−30
−40
−50
−60
−70
[dB]

(a)

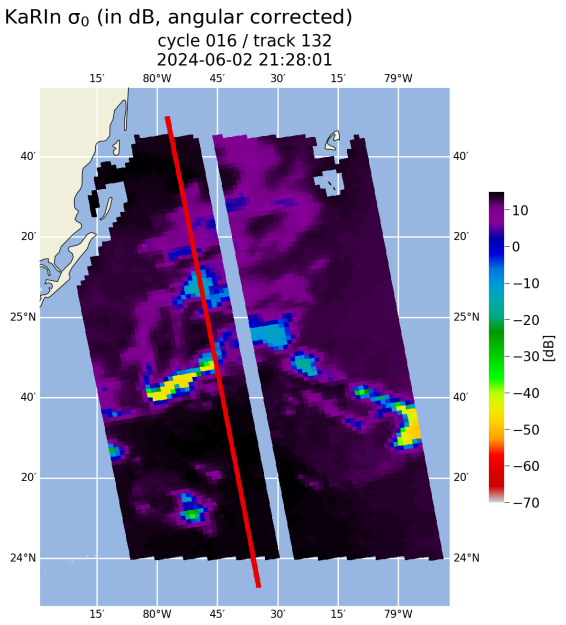
KaRIn σ0 (in dB, angular corrected)
cycle 016 / track 132
2024-06-02 21:28:01
15′ 80°W 45′ 30′ 15′ 79°W
40′
20′
25°N
24°N
10
0
−10
−20
−30
−40
−50
−60
−70
[dB]

(b)

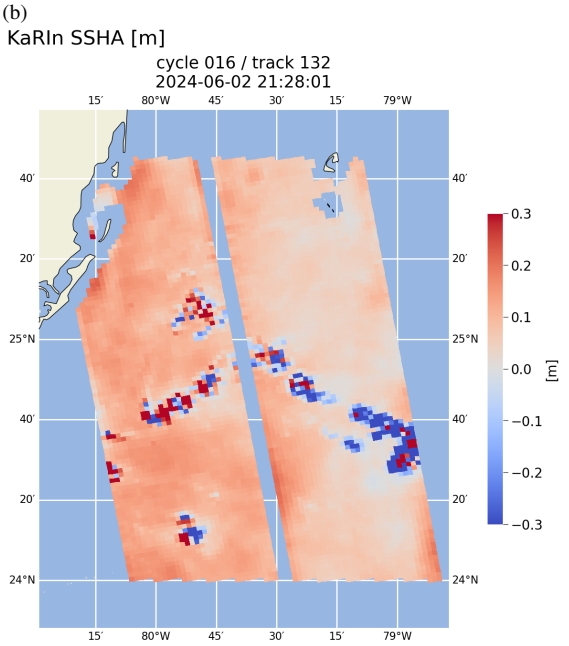
KaRIn SSHA [m]
cycle 016 / track 132
2024-06-02 21:28:01
15′ 80°W 45′ 30′ 15′ 79°W
40′
20′
25°N
24°N
0.3
0.2
0.1
0.0
−0.1
−0.2
−0.3
[m]

(c)

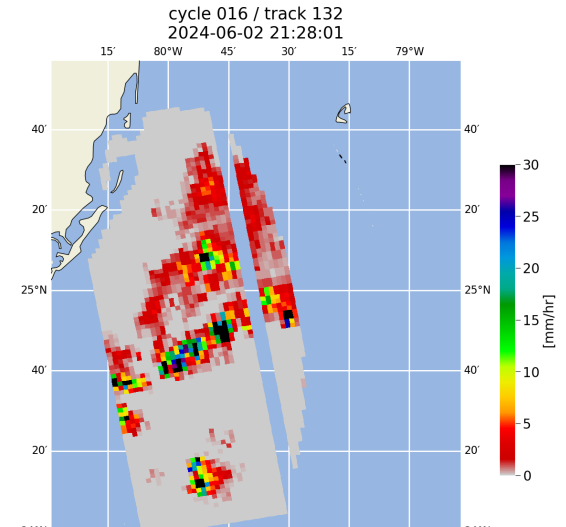
NEXRAD KBYX station rainfall rate
cycle 016 / track 132
2024-06-02 21:28:01
15′ 80°W 45′ 30′ 15′ 79°W
40′
20′
25°N
30
25
20
15
10
5
0
[mm/hr]

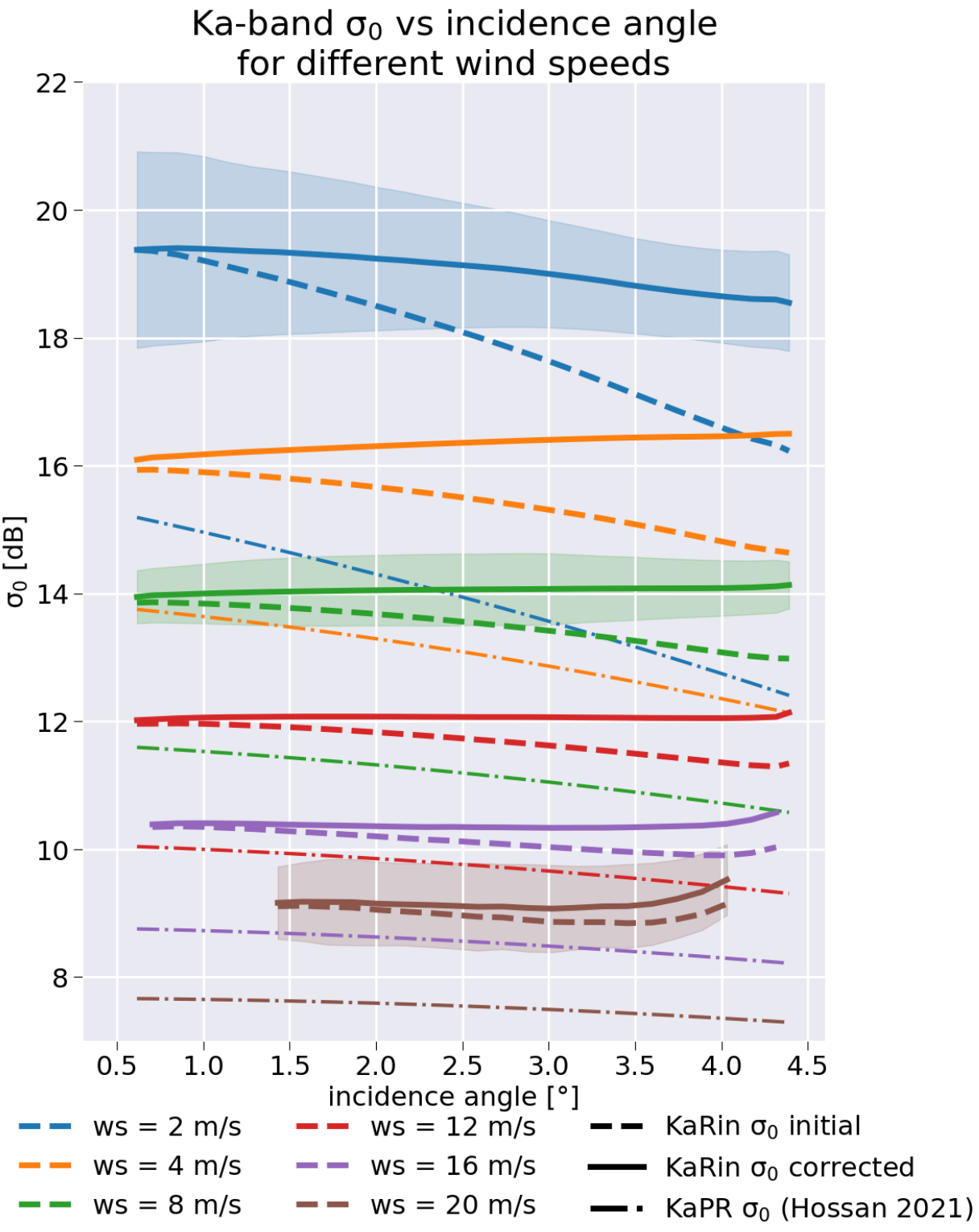

330 FIG. 2. Variation of Ka-band sigma$_0$ with positive incidence angles and wind speeds: σ_0 computed from KaPR
331 GPM (dashed lines, extracted from Hossan and Jones (2021)), the initial KaRin σ_0 (dotted lines) and KaRin
332 angular corrected σ_0 (dotted lines).

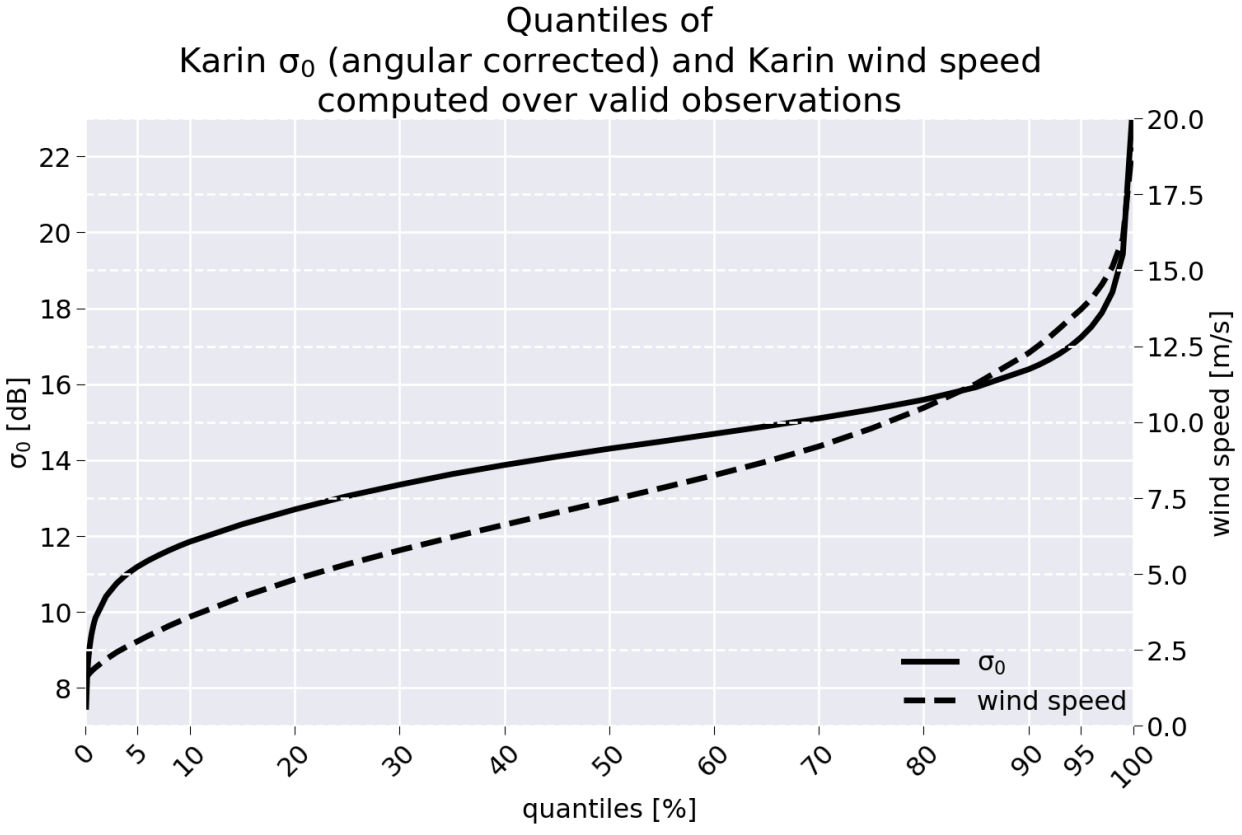

FIG. 3. Quantiles of KaRin sigma$_0$ (solid line) and wind speed (dashed line) computed over valid observations.

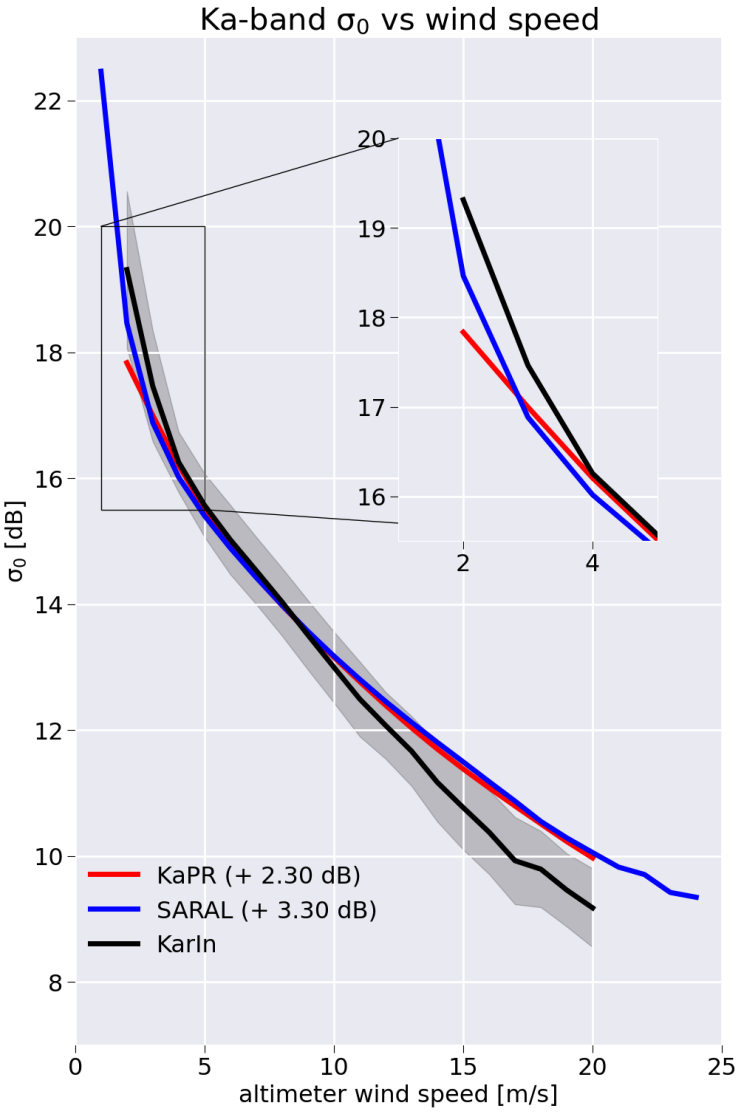

FIG. 4. Variation of Ka-band sigma$_0$ with the wind speed for KaRin (angular corrected, black solid line) GPM KaPR (red line, extracted from Hossan and Jones (2021)) and SARAL altimeter (blue line). The dashed black line shows a fit of the KaRin sigma$_0$ variation with wind speed. A zoom over the 1 m/s - 5 m/s is shown on the upper right part of the figure.

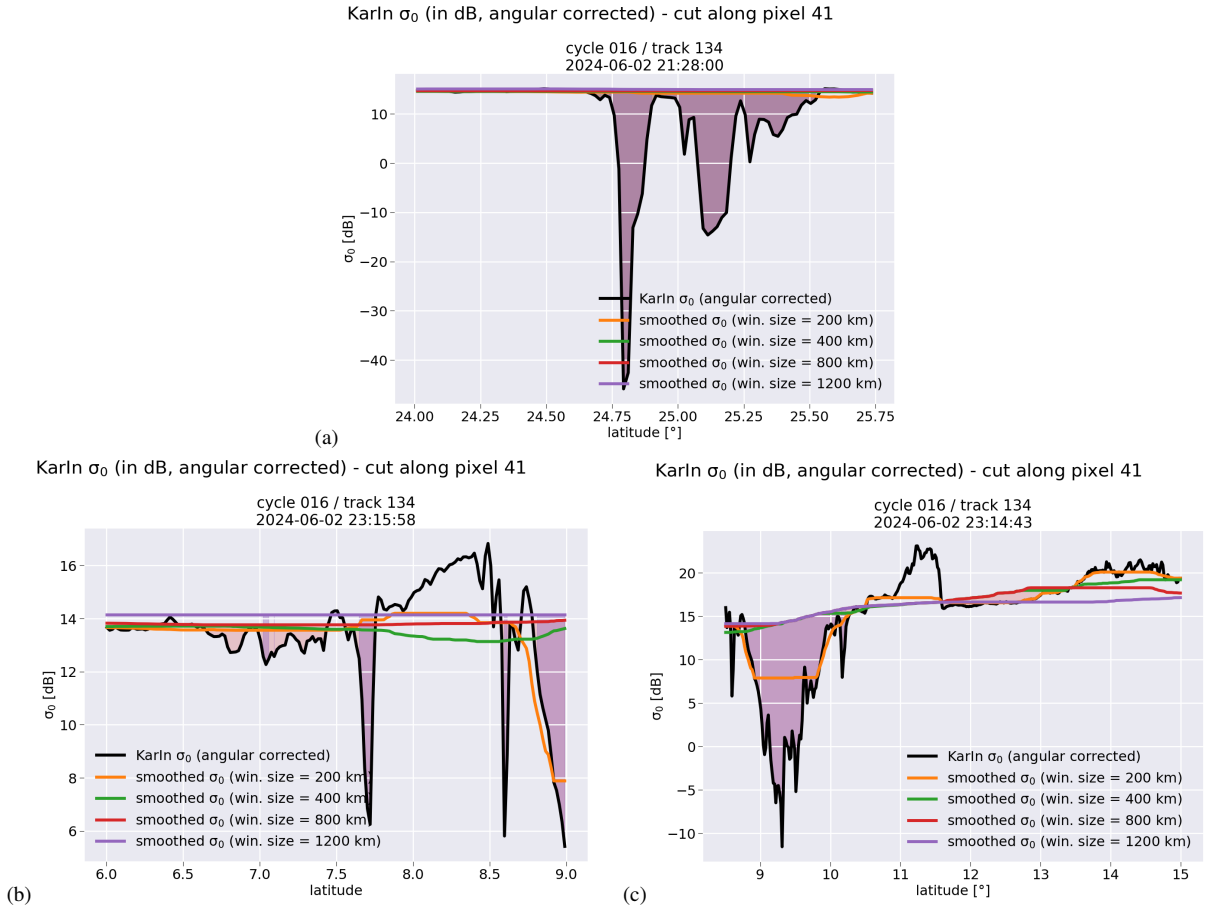

FIG. 5. Illustration of the computation of attenuation using a median filter: cut along the pixel #41 for different atmospheric and surface conditions. The black solid line refers to KaRIn σ_0 in dB and corrected from angular dependency. The orange, green, red and violet solid lines refer to different window size for the median filter, respectively 200 km, 400 km, 800 km and 1200 km. The shaded areas show regions where the attenuation is larger than 0 dB. See the text for more details.

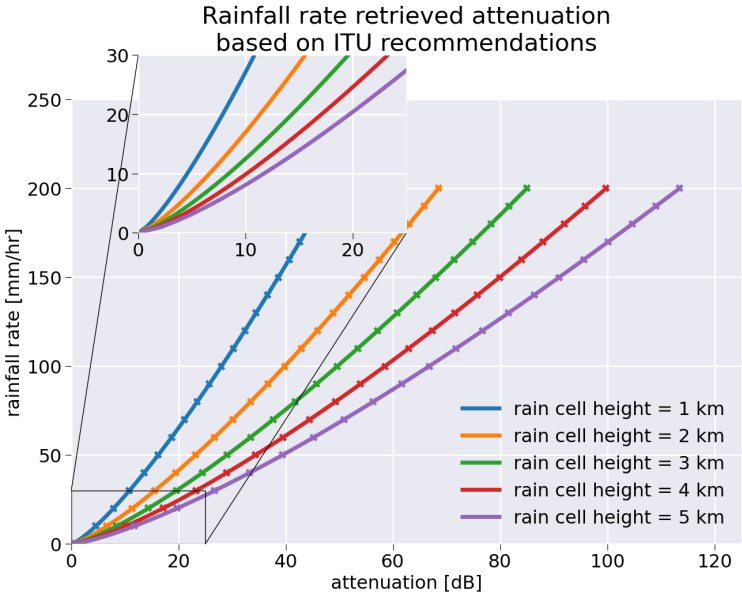

FIG. 6. Rainfall rate retrieved from attenuation and the ITU model. The solid lines show the attenuation computed from the rainfall rates using Eq. 17 for different rain cell heights. The crosses show the fit of the solid lines using a power law.

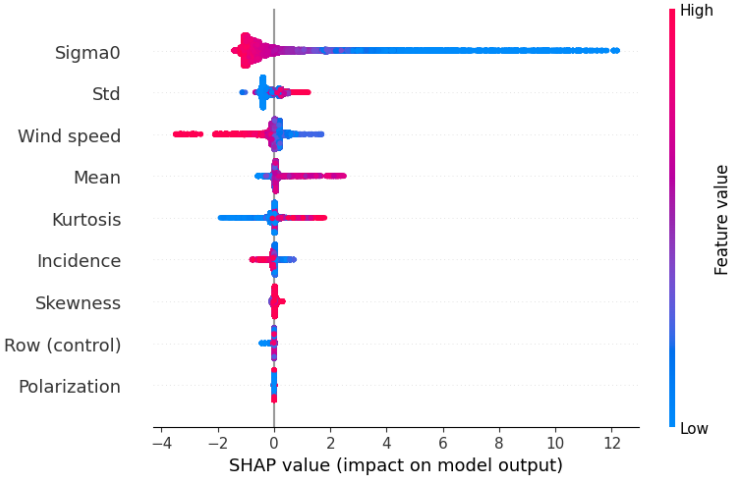

FIG. 7. SHAP value (SHapley Additive exPlanations) for each of the nine input parameters of the random forest algorithm used to retrieve rainfall rate from KaRIn σ_0.

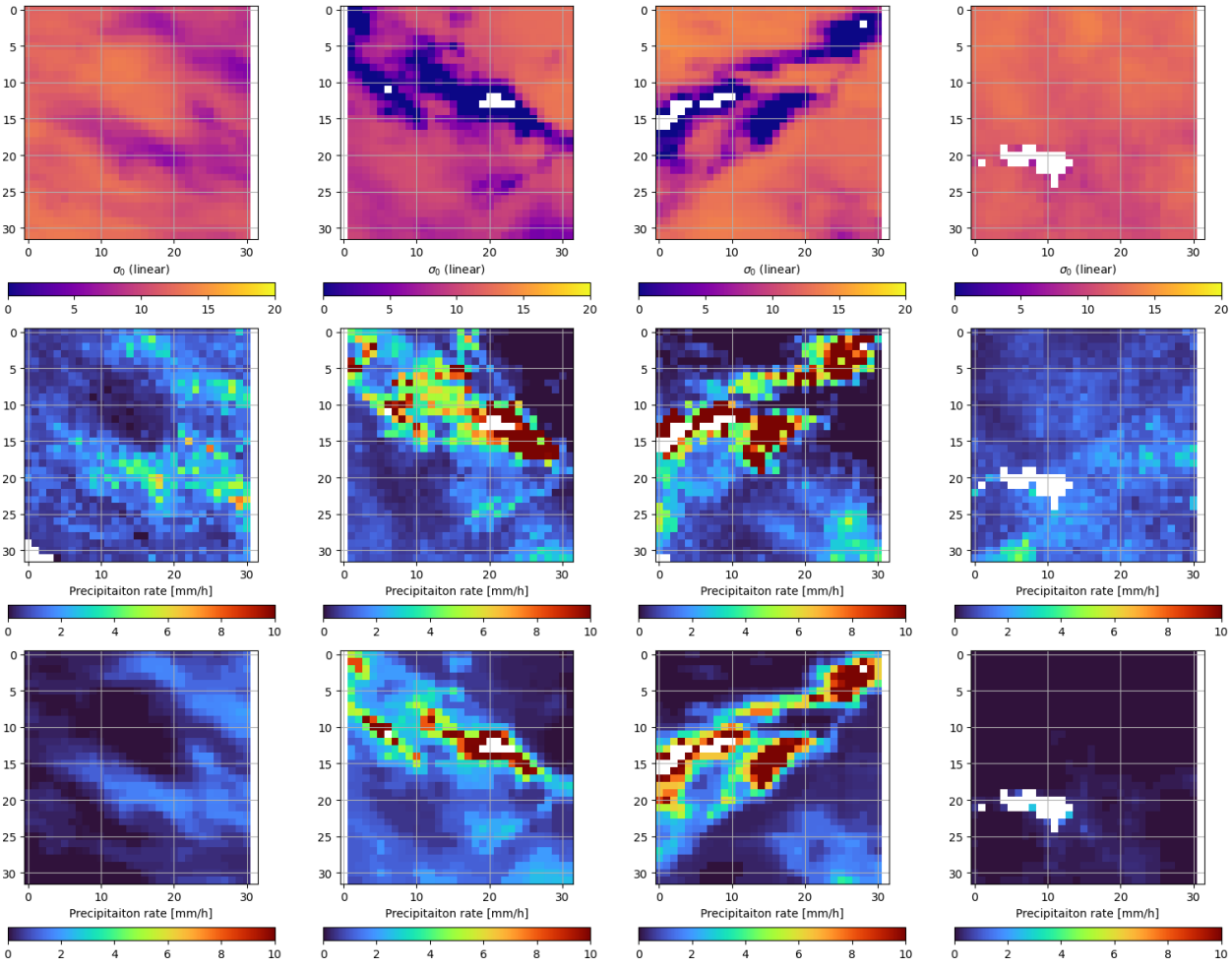

Fig. 8. Comparison of KaRIn backscatter coefficient (σ_0) (top row), collocated NEXRAD rainfall rate (middle row), and predicted rainfall rate based on the random forest approach (R_{RF}) (bottom row) under various precipitation conditions (one per column).

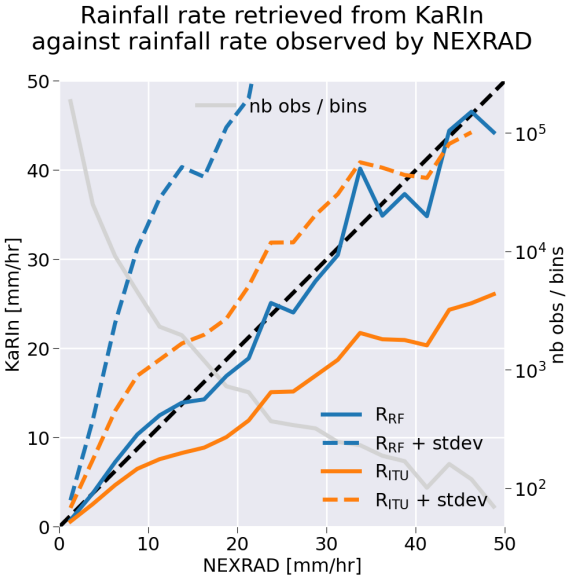

FIG. 9. Mean rainfall rates retrieved from KaRIn σ_0 as a function of NEXRAD rainfall rate, binned in 2.5 mm/hr intervals. The green and orange solid lines correspond respectively to the ITU-based attenuation model (R_{ITU}) and the random forest retrieval (R_{RF}). Dashed lines represent the addition of the standard deviation to each average. The gray line and right-hand y-axis show the number of observations per bin (logarithmic scale).

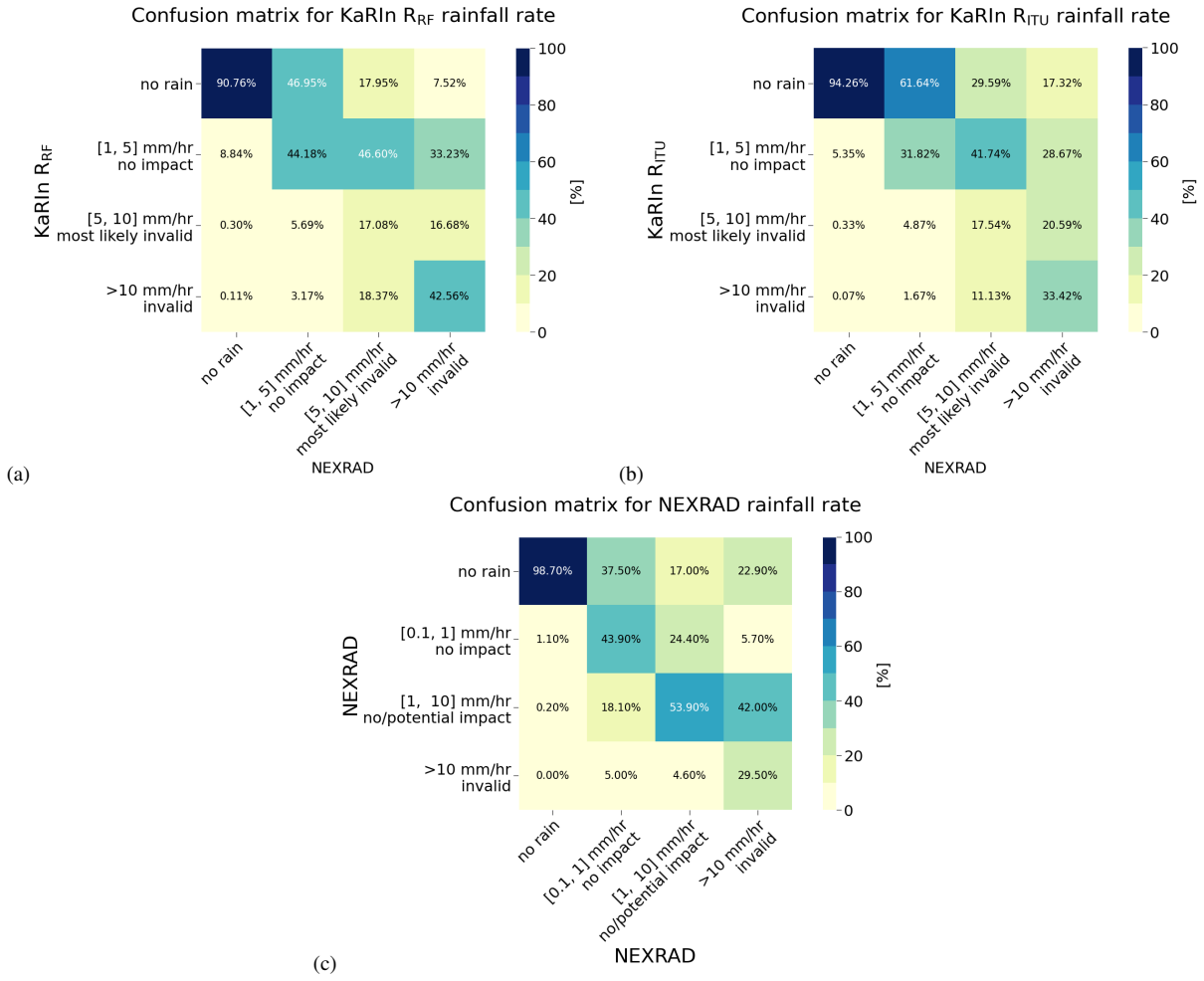

653 FIG. 10. Confusion matrices for the assessment of rainfall rate: a) comparing the retrieval from KaRIn
654 observations based on a random forest approach to NEXRAD, b) comparing the retrieval from KaRIn σ_0 using
655 the ITU-based model to NEXRAD and c) comparing the observations of the same events from two distinct
656 stations of the NEXRAD network.

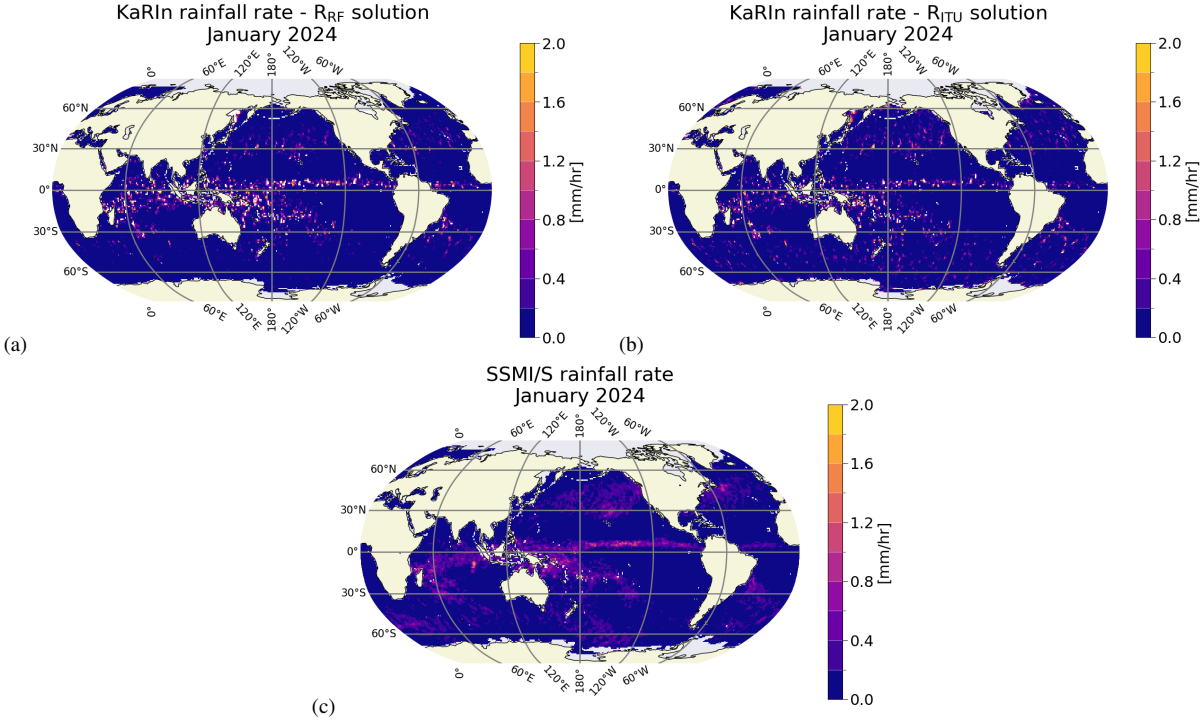

677 FIG. 11. Geographical distribution of monthly mean rainfall rates for January 2024, averaged on a $1° \times 1°$ grid,
678 a) for KaRIn using the random forest approach, b) fro KaRIn using the ITU-bases approach and c) for SSMIS.

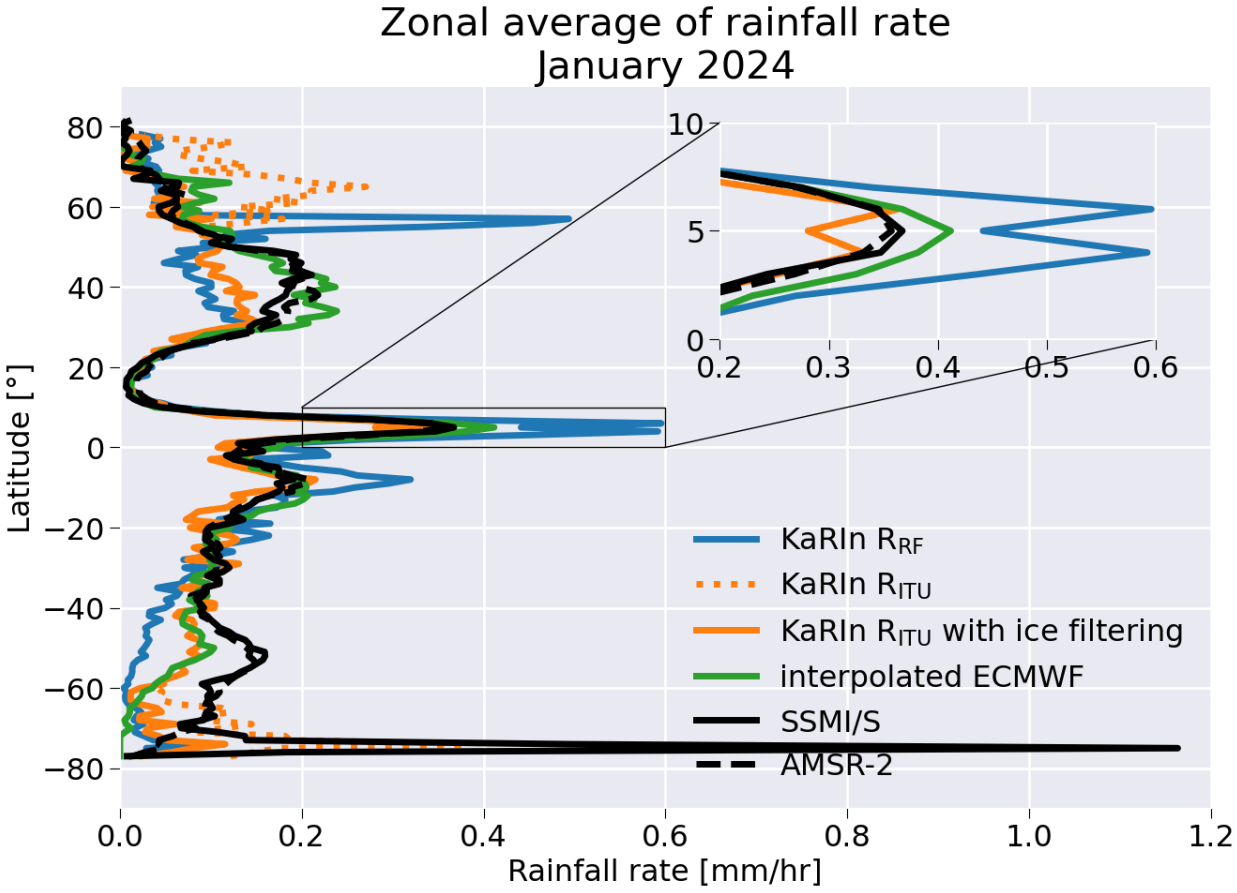

FIG. 12. Zonal distribution of monthly mean rainfall rates for January 2024.

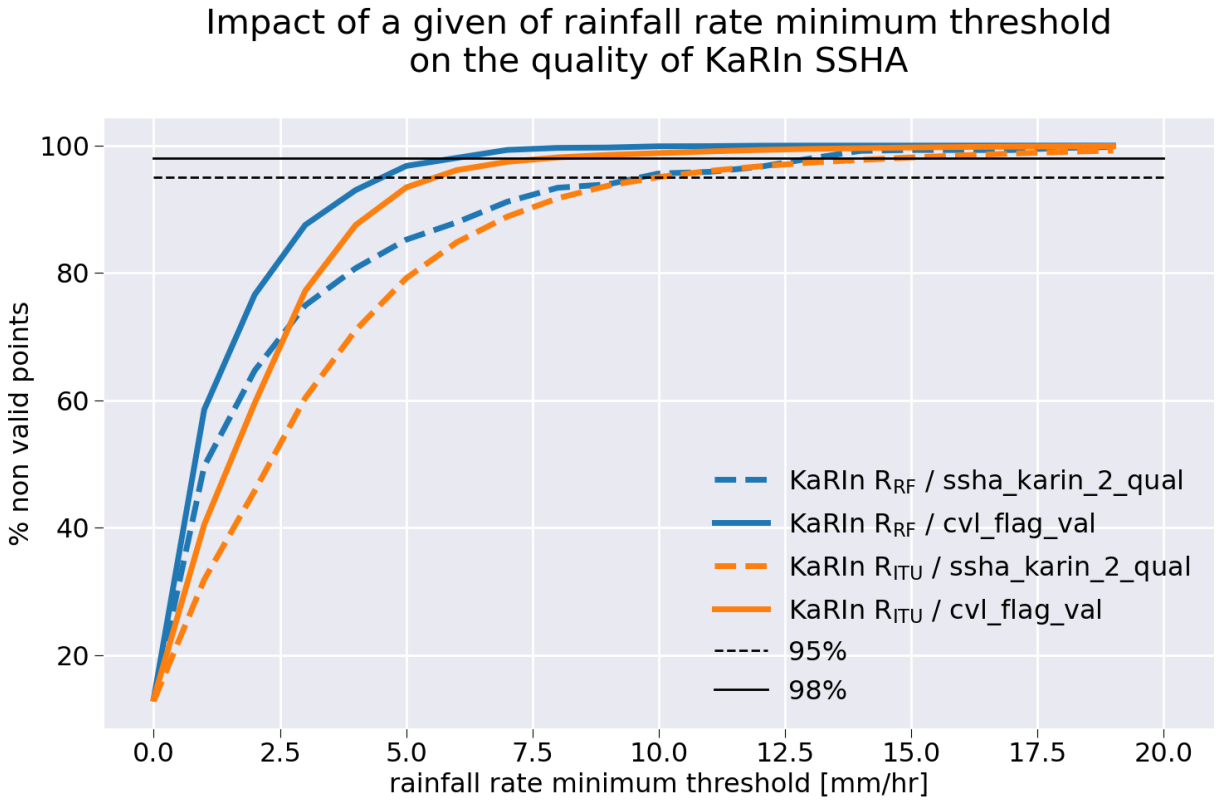

743 FIG. 13. Percentage of invalid SSH measurements as a function of the minimum rainfall rate threshold. Results
744 based on the random forest rain rate estimator (R_{RF}) are shown in blue, while those from the ITU-based model
745 (R_{ITU}) are shown in orange. Dashed lines correspond to the Level-2 quality flag, whereas solid lines correspond
746 to the Level-3 validity flag. The black horizontal dashed and solid lines indicate the 95 % and 98 % invalid data
747 thresholds, respectively.

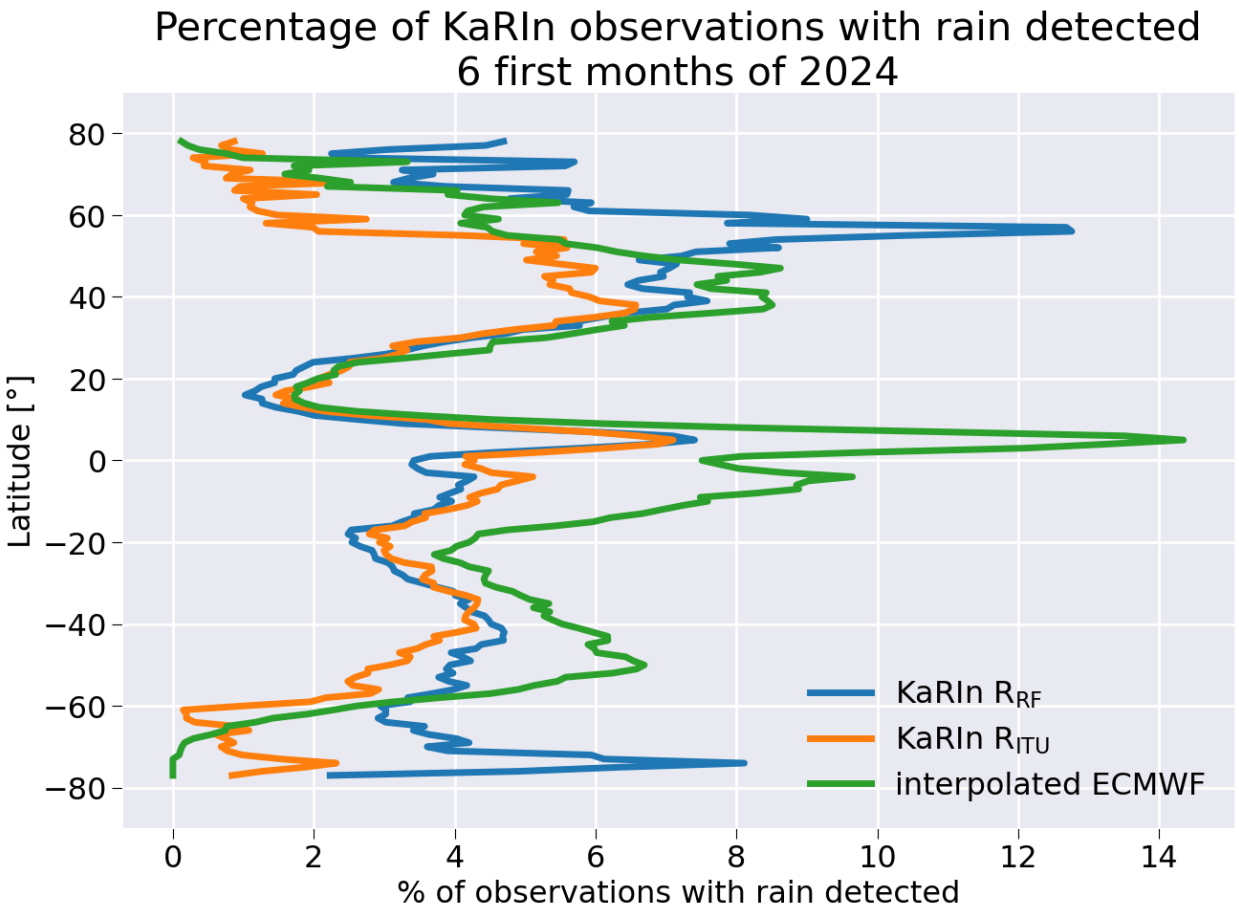

FIG. 14. Percentage of observations for which precipitation has been detected. Results based on the random forest rain rate estimator (R_{RF}) are shown in blue, those from the ITU-based model (R_{ITU}) are shown in orange and those from ECMWF analysis in green.

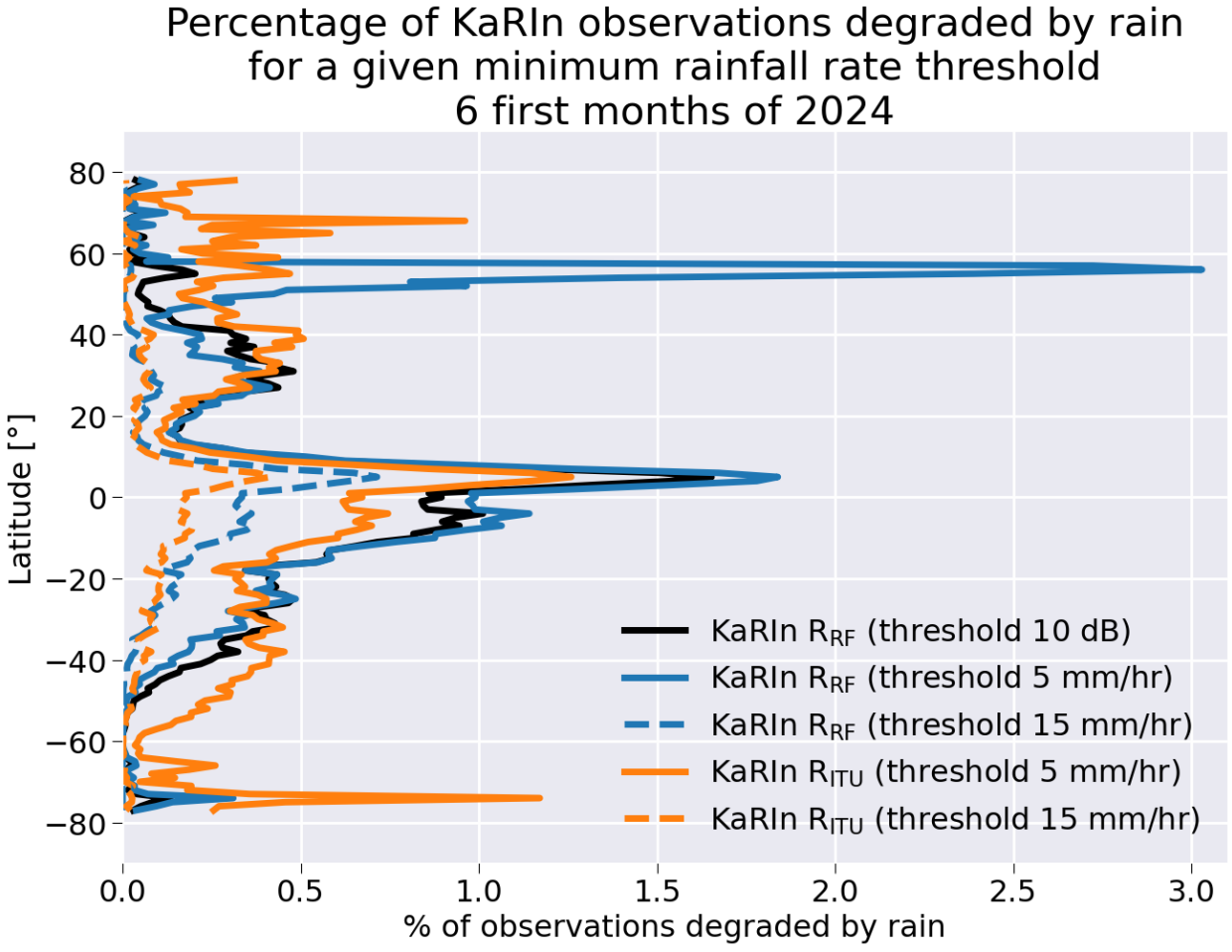

FIG. 15. Percentage of observations for which precipitation has been detected. Results based on the random forest rain rate estimator (R_{RF}) are shown in blue, those from the ITU-based model (R_{ITU}) are shown in orange and those from ECMWF analysis in green.

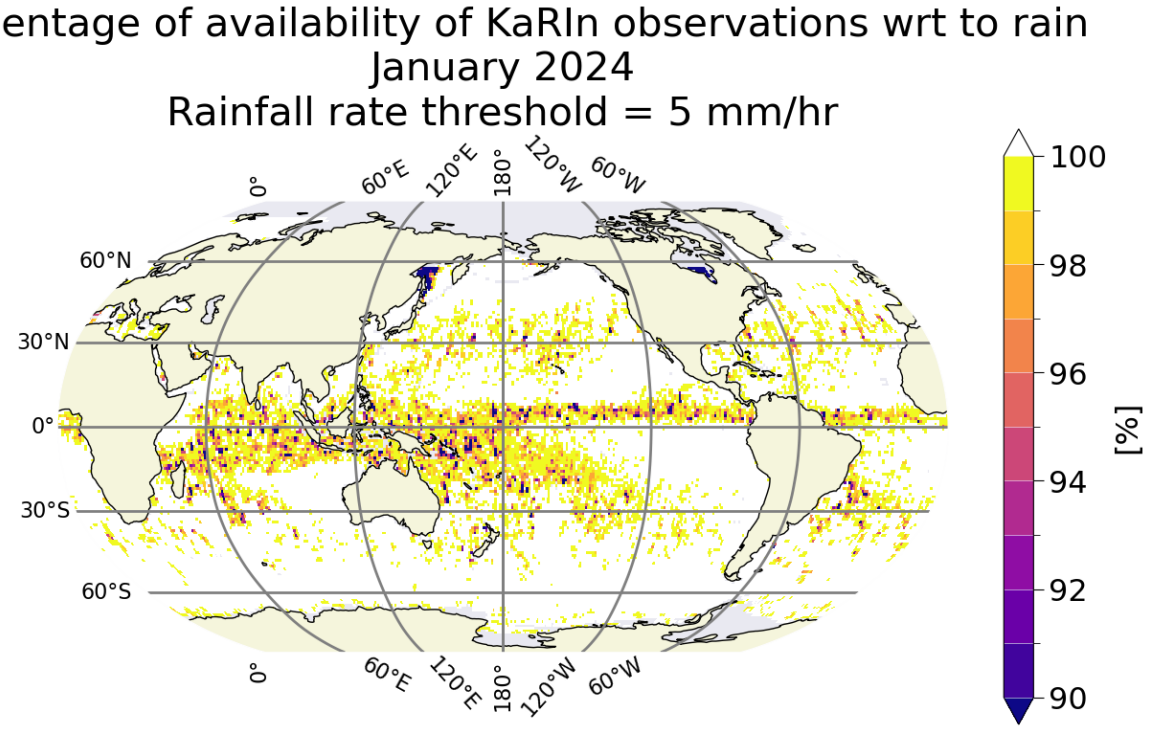

803 FIG. 16. Geographical distribution of the percentage of valid KaRIn observations with respect to rain impact,
804 for a minimum rainfall rate threshold of 5 mm/hr and for January 2024, using the R_{RF} approach.

APPENDIX

From the effect of rain on SWOT KaRIN to the forecast of the observation availability for the future ODYSEA mission.

a. Context

The Ocean Dynamics and Sea Exchanges with the Atmosphere (ODYSEA) mission is a proposed satellite concept designed to provide concurrent and high-resolution observations of ocean surface currents and near-surface winds.

Building on recent advances in Doppler scatterometry, ODYSEA aims to diagnose the wind work at the air–sea interface by resolving the coupled variability of winds and currents across a broad range of spatial and temporal scales Torres et al. (2023).

With a swath width of 1700 km and a spatial resolution of 5 km, ODYSEA is designed to meet the Decadal Survey recommendations for simultaneous measurement of winds and surface currents with revisit times of 12 hours at mid-latitudes. These capabilities position ODYSEA to address key science objectives related to ocean energy pathways, mesoscale eddy dynamics, and atmosphere–ocean coupling.

ODYSEA relies on Doppler scatterometry that operates by measuring the Doppler shift of microwave backscatter from the ocean surface, which carries information about the line-of-sight component of surface motion. By combining observations from multiple azimuth angles within the swath, ODYSEA resolves two-dimensional surface current vectors. Simultaneously, the radar backscatter amplitude is used to estimate near-surface wind speed and direction, following conventional scatterometry principles.

In this appendix, we assess the potential to adapt the methodologies developed for evaluating SWOT KaRIn data availability under precipitation—particularly under Ka-band attenuation effects—for use in the context of ODYSEA. Given that ODYSEA will also operate in Ka-band, lessons from SWOT regarding rain-induced data loss, signal degradation, and spatial heterogeneity of availability are critical for informing expected performance under varying meteorological conditions.

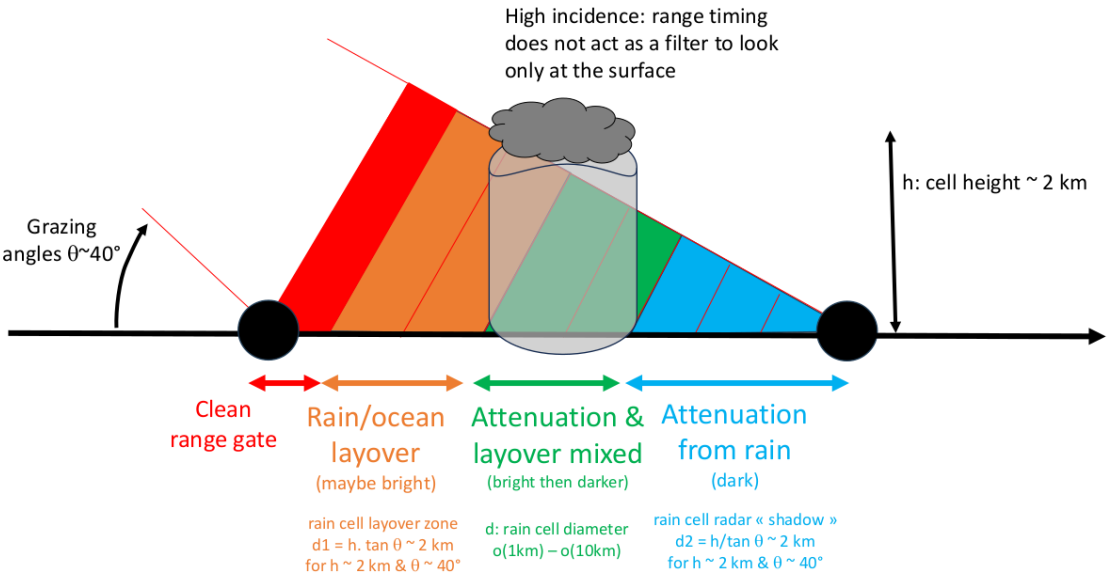

962 FIG. A1. Schematic representation of the geometric configuration of ODYSEA Doppler scatterometric mea-
963 surements in the presence of a convective rain cell.

948 *b. Impact of a rain cell on ODYSEA*

949 The measurement principle of ODYSEA differs fundamentally from that of KaRIn on-board the
950 SWOT mission, as illustrated in Figure A1. ODYSEA employs a rotating Doppler scatterometer
951 that provides multi-azimuthal observations of the sea surface. By design, each surface point within
952 the swath is typically observed at least twice during a single overpass, under a grazing incidence
953 angle of approximately $\theta \sim 40°$.

954 As a result, the impact of a rain cell (depicted as the gray cylinder) is not limited to its nadir
955 projection. On one side, in the direction following the radar line-of-sight, attenuation occurs
956 beyond the rain cell in a so-called shadow region (blue), where the signal is darkened due to the
957 cumulative effect of rain-induced absorption and scattering. On the opposite side, before the rain
958 cell, a brightening effect may appear due to ocean surface layover mixed with backscatter from
959 the rain volume (orange). Within the rain cell itself (green), both attenuation and volumetric
960 backscatter contribute to a more complex signal, typically characterized by a brightening followed
961 by a darkening as the radar beam penetrates and exits the precipitation structure.

964 An accurate estimation of the expected availability rate of ODYSEA measurements in the presence
965 of precipitation would ideally require a dedicated end-to-end simulator, combined with high-

resolution, global-scale atmospheric datasets capable of reproducing the spatial and temporal variability of realistic rain cells. Such a detailed analysis is beyond the scope of the present work. Instead, we propose here a first-order estimation of the ODYSEA data availability based on the observed impact of precipitation on SWOT KaRIn data, using actual measurements.

This extrapolation is performed under the following simplifying assumptions:

- the effect of precipitation on the Ka-band radar signal is assumed to be similar for ODYSEA and KaRIn, as both instruments operate in the same frequency range;
- only geometric aspects of the measurement configurations are considered, without accounting for differences in acquisition geometry or observation dynamics;
- the width of rain cells and the cumulative attenuation along the slant range path are neglected, implying a conservative and schematic approximation of the rain-contaminated areas.

This approach enables a qualitative comparison and provides insight into the potential impact of precipitation on ODYSEA data availability, particularly in regions frequently affected by convective systems.

c. Geometrical Estimation of Rain-Affected Area for ODYSEA Observations

To quantify the potential impact of a rain cell on ODYSEA data availability, we consider the geometric projection of a typical convective rain cell onto the ocean surface, as viewed under ODYSEA's grazing incidence angles ($\theta \sim 40°$).

Assuming a typical rain cell vertical extent $h \sim 2\,\mathrm{km}$ and incidence angle $\theta = 40°$, we can estimate the lateral surface extent of each contaminated zone by simple trigonometric projection:

$$d_{\mathrm{layover}} = h \cdot \tan\theta \approx 2\,\mathrm{km} \cdot \tan(40°) \approx 1.7\,\mathrm{km} \tag{A1}$$

$$d_{\mathrm{shadow}} = \frac{h}{\tan\theta} \approx \frac{2\,\mathrm{km}}{\tan(40°)} \approx 2.4\,\mathrm{km} \tag{A2}$$

Now, if the angle between the successive on-ground observations (forward and backward views) of the same surface pixel is simplified to an idealized orthogonal crossing along the along-track and across-track directions of the KaRIn swath, the effective contamination footprint can be approximated. In this case, each KaRIn pixel identified as invalid due to rain degradation would

propagate its unavailability to the four adjacent pixels in the SWOT 2-km product: one above and one below in the along-track direction, and one to the left and one to the right in the across-track direction. This results in the addition of four extra invalid pixels per rain-contaminated cell, reflecting the impact of multi-directional viewing in the presence of volumetric precipitation effects.

In practice, the following steps are applied to translate the KaRIn data unavailability rate into an estimated ODYSEA data availability:

1. For each SWOT ground track, invalid KaRIn measurements are identified by applying a rain rate threshold of 5 mm/hr on the rain estimate retrieved using the R_{RF} method.

2. For each grid cell flagged as invalid, the typical height of the rain cell is interpolated from the static global map derived from the ITU rain height model, as described in the ITU-R P.839-4 recommendation for propagation prediction methods International Telecommunication Union Radiocommunication Sector (ITU-R) (2013).

3. The number of additional affected pixels corresponding to the layover and shadow zones is computed using Eqs. A1 and A2. These values are converted and rounded to the nearest integer number of 2-km KaRIn pixels. The maximum of the two values is retained and denoted as N.

4. The N neighboring KaRIn pixels in all four cardinal directions (along-track and across-track) surrounding each rain-flagged pixel are then also flagged as invalid.

This approach is illustrated in Figure A2, based on the same example shown in Figure 1. Panel (a) shows the KaRIn pixels initially flagged as invalid because the rainfall rate retrieved by the R_{RF} algorithm exceeds the 5 mm/hr threshold. Panel (b) displays the corresponding rain cell height, interpolated from the ITU-R static map, with most values around 4 km. Panel (c) indicates the number of additional pixels to be flagged, derived from the layover and shadow projections; in this case, three pixels. Finally, panel (d) presents the resulting ODYSEA-flagged pixels, including the original rain-contaminated ones and their surrounding neighbors, as per the geometric expansion described above.

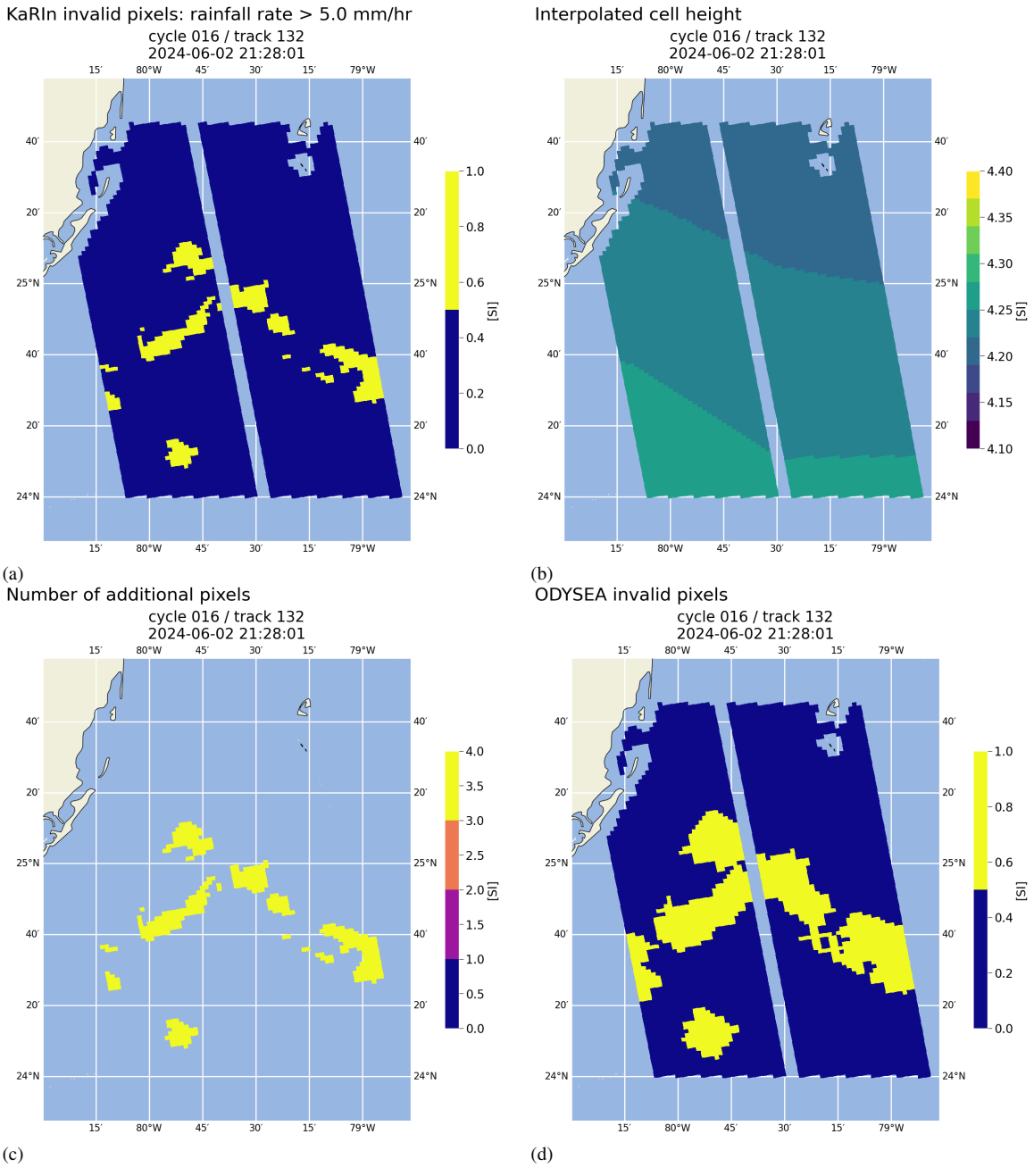

1018 FIG. A2. Illustration of the procedure to extrapolate KaRIn rain-induced unavailability to ODYSEA geometry.
1019 Panel (a) shows the KaRIn pixels flagged as invalid due to high rain rates (>5 mm/hr). Panel (b) displays the
1020 rain cell height interpolated from the ITU-R climatology. Panel (c) shows the number of additional pixels to be
1021 flagged due to layover and shadow effects. Panel (d) presents the final ODYSEA unavailability mask, accounting
1022 for the surrounding affected regions according to the assumptions outlined in the text.

d. Results and conclusions on the availability of ODYSEA measurements with respect to rain degradation

Figure A3 presents the geographical distribution of the expected availability of ODYSEA observations with respect to rain-induced degradation for January 2024. As anticipated, the spatial patterns closely resemble those derived for SWOT KaRIn availability (Figure 16), with more pronounced reductions near the Intertropical Convergence Zone (ITCZ). Despite this, the overall statistics reported in Table **??** indicate that ODYSEA maintains a high level of global availability, with an average of 99.2 %—comparable to KaRIn estimates. Within 10° latitude of the equator, the average availability remains high at 97.3 % in January and 97.0 % in May, underscoring the robustness of the observation capability even in convective regions. Seasonal variations are minimal, with differences between January and May below 0.3 percentage points across all latitudinal bands.

Furthermore, the italicized statistics in Table **??** provide a more nuanced view of data coverage, showing the fraction of grid cells achieving at least 95 % availability. Even in the most impacted tropical zone (within 5° latitude), over 76 % of the grid cells exceed this threshold in January, and nearly 78 % in May. These results suggest that, although precipitation has a measurable impact on data availability in equatorial regions, a substantial fraction of the domain remains reliably observed by ODYSEA under typical rainfall conditions.

In conclusion, under the assumptions and simplifications adopted in this study, the analysis suggests that the ODYSEA mission would satisfy the expected requirement of over 90 % data availability at the global scale, even when accounting for potential degradation due to precipitation. The availability remains particularly high across all latitude bands, including tropical regions where convective rainfall is most frequent. These preliminary findings provide confidence in ODYSEA's robustness with respect to rain-induced limitations. However, these conclusions should be confirmed through future investigations using a dedicated end-to-end simulator that incorporates realistic rain fields, detailed radar signal modeling, and the full instrument acquisition geometry.

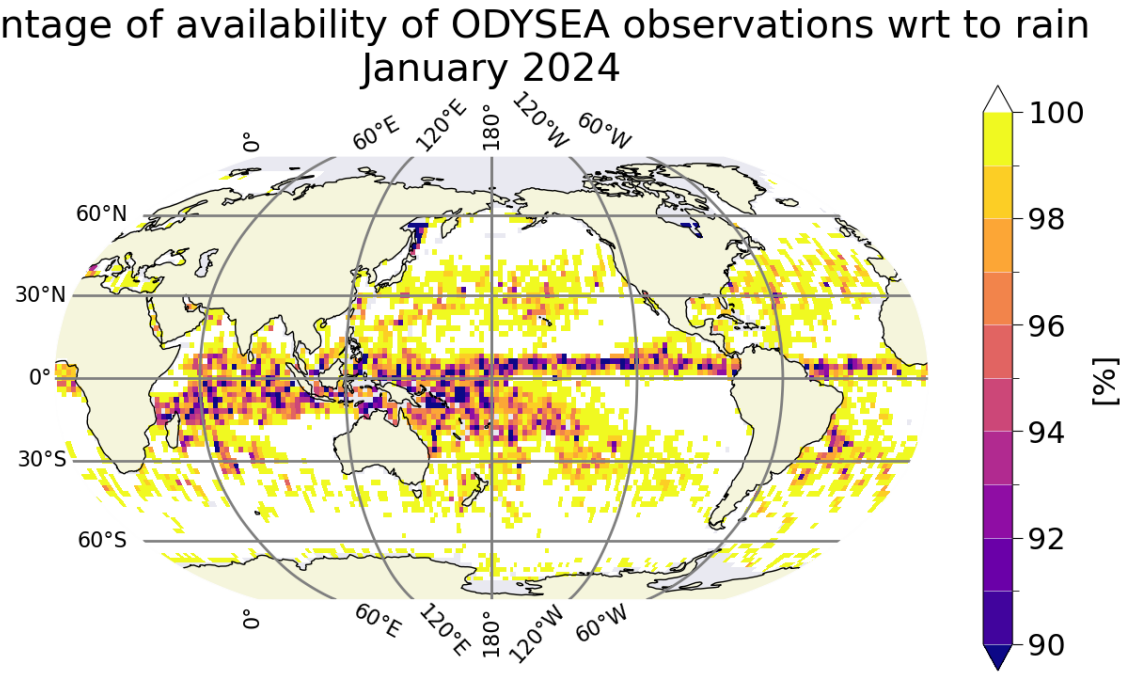

FIG. A3. Geographical distribution of the expected percentage of valid ODYSEA observations with respect to rain impact for January 2024.

References

Alozie, E., and Coauthors, 2022: A review on rain signal attenuation modeling, analysis and validation techniques: Advances, challenges and future direction. MDPI, https://doi.org/10.3390/su141811744.

Bohé, A., 2023: Karin lr oceanography products status & examples. URL https://swotst.aviso.altimetry.fr/fileadmin/user_upload/SWOTST2023/20230919_2_Karin_overview1/11h30-BOHE_plenary.pdf, available online (last access: 12 March 2024), Presented at the 2023 SWOT Science Team meeting (Toulouse).

Chen, C., 2023: Features of karin data that users should be aware of. URL https://swotst.aviso.altimetry.fr/fileadmin/user_upload/SWOTST2023/20230919_3_Karin_overview2/14h10-KaRInFeatures.pdf, available online (last access: 12 March 2024), Presented at the 2023 SWOT Science Team meeting (Toulouse).

Colin, A., and R. Husson, 2024: Rainfall regression from c-band synthetic aperture radar using multi-task generative adversarial networks. *Journal of Applied Earth Observations and Remote Sensing*, https://doi.org/10.1175/AIES-D-24-0007.1, URL https://journals.ametsoc.org/view/journals/aies/4/1/AIES-D-24-0007.1.xml.

Dibarboure, G., and Coauthors, 2024: Blending 2d topography images from swot into the altimeter constellation with the level-3 multi-mission duacs system. *EGU Sphere*, https://doi.org/10.5194/egusphere-2024-1501.

Fu, L.-L., and Coauthors, 2024: The surface water and ocean topography mission: A breakthrough in radar remote sensing of the ocean and land surface water. *Geophysical Research Letters*, **51 (4)**, e2023GL107 652, https://doi.org/10.1029/2023GL107652.

Guymer, T. H., and G. D. Quartly, 1995: Rain effects on ers-1 altimeter data. *Journal of Atmospheric and Oceanic Technology*.

Heiss, W. H., J. W. McGrew, and D. Sirmans, 1990: Nexrad: Next generation weather radar (wsr-88d). *Microwave Journal*, **33**, 79–98.

Hossan, A., and W. L. Jones, 2021: Ku- and ka-band ocean surface radar backscatter model functions at low-incidence angles using full-swath gpm dpr data. *Remote Sensing*, **13 (8)**, 1569, https://doi.org/10.3390/rs13081569, URL https://www.mdpi.com/2072-4292/13/8/1569.

International Telecommunication Union Radiocommunication Sector (ITU-R), 2005: Specific attenuation model for rain for use in prediction methods. Tech. Rep. P.838-3, International Telecommunication Union (ITU), Geneva, Switzerland. URL https://www.itu.int/rec/R-REC-P.838-3-200503-I/en, available online (last access: 12 March 2024).

International Telecommunication Union Radiocommunication Sector (ITU-R), 2013: Recommendation itu-r p.839-4 rain height model for prediction methods. Tech. rep., International Telecommunication Union (ITU), Geneva, Switzerland. URL https://www.itu.int/rec/R-REC-P.839-4-201309-I/en, available online (last access: 12 March 2024).

International Telecommunication Union Radiocommunication Sector (ITU-R), 2022: Recommendation itu-r p.530-18 propagation data and prediction methods required for the design of terrestrial line-of-sight systems p series radiowave propagation. Tech. rep., International

Telecommunication Union (ITU), Geneva, Switzerland. URL https://www.itu.int/rec/R-REC-P.530-18-202109-I/en, available online (last access: 12 March 2024).

Jackson, F. C., W. T. Walton, D. E. Hines, B. A. Walter, and C. Y. Peng, 1992: Sea su'rface mean square slope from k-band backscatter data. 411-422 pp.

Liebe, H. J., H. G., and M. Cotton, 1993: Propagation modeling of moist air and suspended water/ice particles at frequencies below 1000 ghz.

Lillibridge, J., R. Scharroo, S. Abdalla, and D. Vandemark, 2014: One-and two-dimensional wind speed models for ka-band altimetry. *Journal of Atmospheric and Oceanic Technology*, **31**, 630–638, https://doi.org/10.1175/JTECH-D-13-00167.1.

Lundberg, S. M., and S.-I. Lee, 2017: A unified approach to interpreting model predictions. *Advances in Neural Information Processing Systems*, Vol. 30.

Monaldo, F. M., J. Goldhirsh, and E. J. Walsh, 1986: Altimeter height measurement error introduced by the presence of variable cloud and rain attenuation. *Journal of Geophysical Research*, **91**, 2345–2350, https://doi.org/10.1029/JC091iC02p02345.

National Centers for Environmental Information, 2025: Next Generation Weather Radar (NEXRAD). Accessed 26 February 2025, https://www.ncei.noaa.gov/products/radar/next-generation-weather-radar.

National Oceanic and Atmospheric Administration, 2025: NOAA Next Generation Radar (NEXRAD) Level 2 Base Data. Accessed 26 February 2025, https://www.ncei.noaa.gov/metadata/geoportal/rest/metadata/item/gov.noaa.ncdc%3AC00345/html.

Nouguier, F., A. Mouche, N. Rascle, B. Chapron, and D. Vandemark, 2016: Analysis of dual-frequency ocean backscatter measurements at ku-and ka-bands using near-nadir incidence gpm radar data. *IEEE Geoscience and Remote Sensing Letters*, **13**, 1310–1314, https://doi.org/10.1109/LGRS.2016.2583198.

Peral, E., R. Fjørtoft, C. Perigaud, D. Chelton, and E. Rodriguez, 2024: Performance of the swot karin instrument. *Remote Sensing*, **16**, 45, https://doi.org/10.3390/rs16010045.

Picard, B., 2021: Rain cell characterization in ka-band altimetry using swot data. *Remote Sensing*.

Prandi, P., S. Philipps, V. Pignot, and N. Picot, 2015: Saral/altika global statistical assessment and cross-calibration with jason-2. *Marine Geodesy*, **38**, 297–312, https://doi.org/10.1080/01490419.2014.995840.

Quartly, G. D., 1998: Estimating rain rates using altimeter data. *Journal of Atmospheric and Oceanic Technology*.

Raynal, M., and Coauthors, 2023: Early swot 21-day data assessment. URL https://swotst.aviso.altimetry.fr/fileadmin/user_upload/SWOTST2023/20230922_1_going_forward/09h10-RAYNAL_L2LR_CalVal_scienceOrbit.pdf, available online (last access: 12 March 2024), Presented at the 2023 SWOT Science Team meeting (Toulouse).

Srokosz, M. A., 1988: The effect of rain on seasat radar altimeter data. *IGARSS Proceedings*.

SWOT Project Science Team, 2018: Swot science requirements document, rev b. Tech. Rep. JPL D-61923, Jet Propulsion Laboratory, California Institute of Technology. Version B, January 24, 2018.

Torres, H., A. Wineteer, P. Klein, T. Lee, J. Wang, E. Rodriguez, D. Menemenlis, and H. Zhang, 2023: Anticipated capabilities of the odysea wind and current mission concept to estimate wind work at the air–sea interface. *Remote Sensing*, **15 (13)**, 3337, https://doi.org/10.3390/rs15133337.

Tournadre, J., 1998: Detailed analysis of rain cell characteristics from topex data. *Journal of Atmospheric and Oceanic Technology*.

Tournadre, J., 2009: Rain attenuation in the ka-band for altimeter missions. *IEEE Transactions on Geoscience and Remote Sensing*.

Tournadre, J., J. C. Poisson, and B. Picard, 2015: Rain flagging for altika using matching pursuit. *Marine Geodesy*.

Vandemark, D., B. Chapron, H. Feng, and A. Mouche, 2016: Sea surface reflectivity variation with ocean temperature at ka-band observed using near-nadir satellite radar data. *IEEE Geoscience and Remote Sensing Letters*, **13**, 510–514, https://doi.org/10.1109/LGRS.2016.2520823.

Wentz, F., K. Hilburn, and D. Smith, 2012: Remote sensing systems dmsp ssmis monthly environmental suite on 0.25 deg grid, version 8. Tech. rep., Remote Sensing Systems, Santa Rosa, CA. URL www.remss.com/missions/ssmi, available online (last access: 31 March 2024).

Yan, Q., J. Zhang, C. Fan, and J. Meng, 2019: Analysis of ku- and ka-band sea surface backscattering characteristics at low-incidence angles based on the gpm dual-frequency precipitation radar measurements. *Remote Sensing*, **11**, 754, https://doi.org/10.3390/rs11070754.